The 2020 Mw 6.5 Monte Cristro Range (Nevada) earthquake: anatomy of a large rupture through a region of highly-distributed faulting

Sethanant Israporn[1], Nissen Edwin[1], Pousse-Beltran Léa[2], Bergman Eric A[3], and Pierce Ian[4]

[1]University of Victoria
[2]School of Earth and Ocean Sciences, University of Victoria, Victoria, British Columbia, Canada- Univ. Grenoble Alpes, Univ. Savoie Mont Blanc, CNRS, IRD, UGE, ISTerre, 38000 Grenoble, France
[3]Global Seismological Services
[4]University of Oxford

November 16, 2022

Posted on 16 Nov 2022 — CC-BY 4.0 — https://doi.org/10.1002/essoar.10511959.1 — This a preprint and has not been peer reviewed. Data may be preliminary.

Abstract

The 15 May 2020 Mw 6.5 Monte Cristo Range earthquake (MCRE) in Nevada, USA is the largest instrumental event in the Mina deflection, an E-trending stepover zone of highly diffuse faulting within the Walker Lane. The MCRE mostly ruptured previously unmapped faults, motivating us to characterize the behaviour of an earthquake on a structurally-immature fault. We use Interferometric Synthetic Aperture Radar (InSAR) data and regional GNSS offsets to model the causative faulting. Our three fault model indicates almost pure left-lateral motion in the east and normal-sinistral slip in the west. Maximum slip of 1.1 m occurs at 8-10 km depth but less than 0.2 m of slip reaches the surface, yielding a pronounced shallow slip deficit (SSD) of 86%. Our calibrated relocated hypocenters and focal mechanisms indicate that the mainshock initiated at 9 km depth and aftershock focal depths range from 1 to 11 km, helping constrain the local seismogenic thickness. We further present new field observations of fracturing and pebble-clearing that shed light on the western MCRE kinematics, revealing a paired fault system below the spatial resolution of the InSAR model. The segmented fault geometry, off-fault aftershocks with variable mechanisms, distributed surface fractures, limited long-term geomorphic features, and an estimated cumulative offset of 600-700 m, are all characteristic of a structurally-immature fault system. However, the large SSD is not unusual for an earthquake of this magnitude, and a larger compilation of InSAR models (twenty-eight Mw[?]6.4 strike-slip events) shows that SSDs are not correlated with structural maturity as previously suggested.

The 2020 M_w 6.5 Monte Cristro Range (Nevada) earthquake: anatomy of a large rupture through a region of highly-distributed faulting

Israporn Sethanant[1], Edwin Nissen[1], Léa Pousse-Beltran[1,2], Eric Bergman[3], Ian Pierce[4]

[1]School of Earth and Ocean Sciences, University of Victoria, British Columbia, Canada
[2]Institut des Sciences de la Terre, Université Grenoble Alpes, Université Savoie Mont Blanc, CNRS, IRD, 38000 Grenoble, France
[3]Global Seismological Services, Golden, Colorado, USA
[4]Department of Earth Sciences, University of Oxford, United Kingdom

Key Points:

- The mainshock exhibits complex faulting with oblique and pure sinistral slip in the western and eastern fault sections, respectively
- Segmented faulting, off-fault deformation, and aftershocks with variable mechanisms are consistent with rupture on an immature fault
- However, earthquake magnitude may have a stronger influence on shallow slip deficit than fault structural maturity

Corresponding author: Israporn Sethanant, isethanant@uvic.ca

Abstract

The 15 May 2020 M_w 6.5 Monte Cristo Range earthquake (MCRE) in Nevada, USA is the largest instrumental event in the Mina deflection, an E-trending stepover zone of highly diffuse faulting within the Walker Lane. The MCRE mostly ruptured previously unmapped faults, motivating us to characterize the behaviour of an earthquake on a structurally-immature fault. We use Interferometric Synthetic Aperture Radar (InSAR) data and regional GNSS offsets to model the causative faulting. Our three fault model indicates almost pure left-lateral motion in the east and normal-sinistral slip in the west. Maximum slip of 1.1 m occurs at 8–10 km depth but less than 0.2 m of slip reaches the surface, yielding a pronounced shallow slip deficit (SSD) of 86%. Our calibrated relocated hypocenters and focal mechanisms indicate that the mainshock initiated at 9 km depth and aftershock focal depths range from 1 to 11 km, helping constrain the local seismogenic thickness. We further present new field observations of fracturing and pebble-clearing that shed light on the western MCRE kinematics, revealing a paired fault system below the spatial resolution of the InSAR model. The segmented fault geometry, off-fault aftershocks with variable mechanisms, distributed surface fractures, limited long-term geomorphic features, and an estimated cumulative offset of 600–700 m, are all characteristic of a structurally-immature fault system. However, the large SSD is not unusual for an earthquake of this magnitude, and a larger compilation of InSAR models (twenty-eight $M_w \geq$6.4 strike-slip events) shows that SSDs are not correlated with structural maturity as previously suggested.

Plain Language Summary

The 2020 Monte Cristo Range earthquake, western Nevada, ruptured mostly previously unrecognized faults in a highly fractured region of crust in which no single, through-going fault has yet emerged. Understanding the behaviour of an earthquake in such regions is crucial for assessing their seismic hazard. We use radar satellite imagery and GPS measurements to model the fault geometry of the earthquake, and how much slip occurred. We found that only ∼15% of the slip at depth reached the surface. We also use seismograms to estimate the nucleation depth and aftershock patterns. Results show that the earthquake sequence involved a variety of fault orientations and movements. We further integrate field observations of surface cracks, which revealed even more complicated structures and movements in the western rupture zone. The segmented fractures, distributed aftershocks and their varied geometries, and the limited record of past earthquakes, are all characteristics of a newly emergent fault zone. However, according to our comparison with twenty-seven other global earthquakes, the small proportion of slip that reached the surface does not relate with the faults being new, but rather the size of the earthquake.

1 Introduction

Fault segmentation is known to play an important role in earthquake rupture propagation and arrest. The influential 'characteristic earthquake' model posits that maximum earthquake magnitudes are limited by the lengths of discrete, mapped fault segments and their intervening segment boundaries (Schwartz & Coppersmith, 1984; Wesnousky, 2006). However, in recent years this simple view has been complicated by observations of a number of multi-fault earthquakes that have jumped across major segment boundaries to achieve larger rupture areas and magnitudes than would normally be anticipated (e.g., Hicks & Rietbrock, 2015; Huang et al., 2016; Nissen et al., 2016; Hamling et al., 2017). Fault segmentation is one manifestation of fault structural maturity, a term that describes the evolution of fault zone properties with incremental offset. In this progression, a fault core thickens (e.g., Robertson, 1983; Scholz, 1987; Hull, 1988; Childs et al., 2009), off-fault damage intensifies (e.g., Shipton & Cowie, 2001; Finzi et al., 2009; Faulkner et al., 2011; Savage & Brodsky, 2011; Aben et al., 2016), and the fault trace simplifies as segments coalesce and asperities are smoothed out (e.g., Walsh & Watterson, 1988; Wesnousky, 1988; Peacock & Sanderson, 1991; Childs et al., 1995; Stirling et al., 1996; Frost et al., 2009; Wechsler et al., 2010; Brodsky et al., 2011). Other aspects of structural maturity may also be important in controlling earthquake rupture behaviour. Observations suggest that earthquakes along structurally-mature faults exhibit more localized deformation and narrower aftershock distributions (Powers & Jordan, 2010; Zinke et al., 2015; Hatem et al., 2017; Perrin et al., 2021), faster rupture velocities (Perrin et al., 2016; Chounet et al., 2018), more persistent rupture directivity (Kane et al., 2013; Aderhold & Abercrombie, 2015), proportionally more surface slip (Dolan & Haravitch, 2014), larger amounts of aseismic afterslip (Johanson et al., 2006; L. Feng et al., 2010; Thomas et al., 2014; Y. Li et al., 2020; Pousse-Beltran et al., 2020), smaller overall stress drops and weaker near-field ground motions (Choy & Kirby, 2004; Radiguet et al., 2009; Hecker et al., 2010), and lower rates of dynamic aftershock triggering (Gomberg, 1996), than those along immature faults. Mature faults may also exhibit steadier interseismic strain accumulation (K. Wang et al., 2021) and more regular recurrence intervals (Berryman et al., 2012; Thakur & Huang, 2021).

These relationships illustrate how the structural setting of an earthquake, including fault segmentation and structural maturity, could have an important bearing on seismic hazard. They raise the possibility of incorporating easily-observed metrics for structural maturity—such as fault cumulative offset, age, slip rate, length, and surface trace complexity (Choy & Kirby, 2004; Manighetti et al., 2007, 2021)—in hazard assessments and earthquake early warning algorithms (Dolan & Haravitch, 2014; Perrin et al., 2016; Hutchison et al., 2020). However, other factors including fault geometry and kinematic style, tectonic environment, and rheology of ruptured material may also influence earthquake behaviour, potentially complicating matters (e.g., Oskin et al., 2012; Teran et al., 2015). To clarify these relations further, careful observations are needed of earthquakes from a range of structural and geological settings and which span the full spectrum of fault structural maturity.

The M_w 6.5 Monte Cristo Range earthquake (MCRE) ruptured on 15 May 2020 at 11:03 UTC (4:03 AM local time) mostly along previously unmapped faults in the Mina deflection zone within the central Walker Lane, Nevada (Wesnousky, 2005) (Figure 1). The evolution of the Mina deflection since the Miocene has given rise to a region of conspicuously heterogeneous lithology and geometrically complex faulting (Wetterauer, 1977; Oldow et al., 1994, 2008). Fault segments mapped in the western Mina deflection, just west of the MCRE, are relatively short (on average 1–3 km) with a maximum segment length of ∼10 km, highly distributed, and variably oriented (Dohrenwend, 1982; Oldow et al., 1994), and some reactivate inherited structures (Wetterauer, 1977; Oldow et al., 2008). Faults and fault-bound blocks within the Mina deflection are thought to rotate about vertical axes to accommodate dextral shear transfer across the Walker Lane (Wesnousky, 2005). This crustal rotation potentially diverts the faults away from being favorable to slip, preventing the emergence of a single through-going fault that could attain structural maturity. Following the mainshock, field mapping revealed zones of distributed fractures within an approximately 28 km-long and up to 800 m wide rupture zone (Koehler et al., 2021). This distributed deformation, together with the slow rupture velocity (Liu et al., 2021), extensive off-fault aftershocks (Ruhl et al., 2021), and the weakly discernible neotectonic landforms indicative of long-term faulting (Koehler et al., 2021), also suggest that the MCRE may have ruptured a highly-immature fault system.

In this study, we carefully characterize the MCRE to further illuminate its rupture behaviour. We use Interferometric Synthethic Aperture Radar (InSAR) and seismology to model the source geometry and kinematics. Near-field observations of fault offsets and off-fault deformation are integrated to shed light on the complex block motions within the fault zone. We discuss these results in the context of fault structural maturity and show that various attributes of the MCRE are characteristic of rupture within an emergent and highly-distributed fault system. We further highlight the importance of incorporating multi-disciplines to capture the full complexity of a rupture especially in a shattered crustal zone.

2 Regional Context

The Walker Lane lies between the Sierra Nevada block and the Basin and Range extensional province (Locke et al., 1940; Stewart & Ernst, 1988) and accommodates ∼20% of the ∼50 mm/yr dextral motion between the Pacific and North America Plates (Dokka & Travis, 1990; Bennett et al., 2003). This shear is distributed across an array of NW-trending dextral faults, N- to NE-trending normal faults, and NE-striking sinistral faults (Wesnousky, 2005). Several of these faults have hosted large historic earthquakes, including the 1954 M_s 7.2 Fairview Peak, 1932 M_w 6.8 Cedar Mountain, and 1872 M 7.6 Owens Valley earthquakes (Hodgkinson et al., 1996; Wesnousky, 2005) (Figure 1). The Mina deflection zone located within the central Walker Lane, however, comprises a suite of discontinuous E-W faults, disrupting the overall northerly-oriented structures of the Walker Lane (Pierce et al., 2021). The left-lateral faults of the Mina deflection accommodate a ∼25–60 km-wide right step that help transfer dextral slip between the longer, NW-striking, dextral White Mountain and Fish Lake Valley fault zones to the southwest and the Benton Springs and Petried Springs faults to the northeast (Wesnousky, 2005; Lee et al., 2009; DeLano et al., 2019). To accommodate this strain transfer, most geologic, geomorphic, geodetic, and paleomagnetic analyses suggest that the Mina deflection is dominantly occupied by E-W sinistral faults that rotate clockwise around vertical axes, opening small, triangular basins at the fault termini (Wesnousky, 2005; Petronis et al., 2009; Rood et al., 2011; Nagorsen-Rinke et al., 2013; Bormann et al., 2016; Grondin et al., 2016; DeLano et al., 2019; Pierce et al., 2021).

The Mina deflection is comprised to the first order of a series of E-striking sinistral faults, including from north to south the Rattlesnake, Excelsior, Candelaria, and Coaldale faults (Figure 1). Each of these faults is made up of numerous discrete segments that sum to lengths of up to ∼20 km (Wesnousky, 2005). In general, the faults exhibit alternating north- and south-facing vertical scarps, geomorphic marker offsets, linear fault-bounded ridges, *en echelon* fractures and pressure ridges, and beheaded stream channels within bedrock and Quaternary alluvium, indicative of sinistral and normal faulting (Wesnousky, 2005; Lee et al., 2006). The only historic earthquake in this area is the 1934 M_w 6.3 Excelsior Mountain earthquake which produced *en echelon* fissures and down-to-the-north vertical scarps along the Excelsior fault, consistent with normal-sinistral slip (Callaghan & Gianella, 1935; Wesnousky, 2005).

The MCRE is the largest instrumentally-recorded earthquake in the Mina deflection. The mainshock ruptured areas where E-trending Quaternary faults have not been mapped, as well as sections where the rupture projects into the NW-striking Benton Springs and Petrified Springs faults in the north (Koehler et al., 2021). In the west, the MCRE ruptured the eastern projection of the Candelaria fault. Although there are no historic earthquakes along the Candelaria fault, it exhibits evidence for surface ruptures in the middle to late Holocene (Wesnousky, 2005), with a net sinistral-normal slip of ∼900 m since 2.8 Ma, measured from offset markers of Pliocene basalt, for an approximate Quaternary slip rate of 0.3 mm/yr (Speed & Cogbill, 1979).

3 Data and Methodology

3.1 InSAR and GNSS Data and Processing

We produced three six-day interferograms using SAR images acquired by the European Space Agency's C-band (wavelength 5.6 cm) Sentinel-1 satellites. The SAR im-

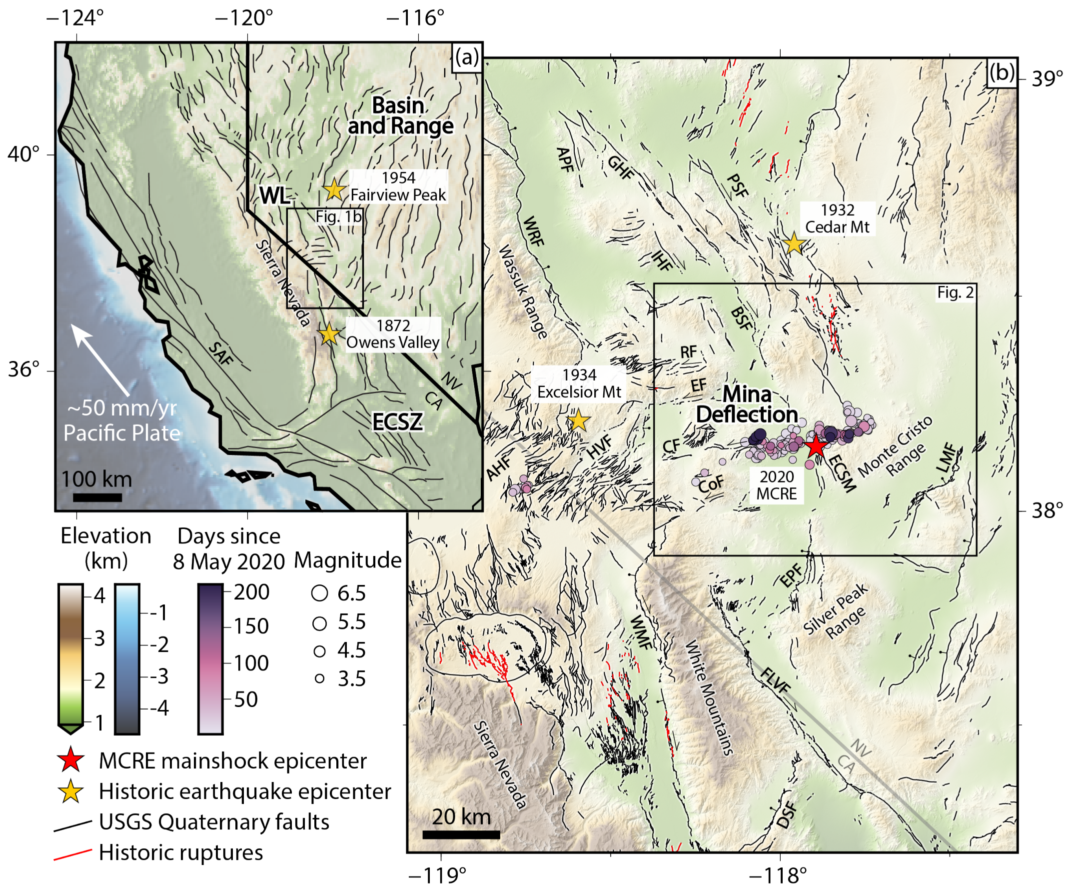

Figure 1. Tectonic setting of the 2020 Monte Cristo Range earthquake. (a) Regional context of the Eastern California shear zone (ECSZ) and Walker Lane (WL) and (b) a zoom in of the Walker Lane. The red star is our relocated MCRE mainshock epicenter and yellow stars indicate the 1872 M 7.6 Owens Valley, 1932 M_w 6.8 Cedar Mountain, 1934 M_w 6.3 Excelsior Mountain, and the 1954 M_s 7.2 Fairview Peak earthquake epicenters (from the NEIC and Callaghan and Gianella (1935)). The circles in (b) are relocated epicenters of the MCRE sequence, scaled with magnitude, and shaded with the number of days since 8 May 2020. Major faults (black lines) and historic ruptures (red lines): AHF—Anchorite Hills fault; APF—Agai Pah fault; BSF—Benton Springs fault; CF—Candelaria fault; CoF—Coaldale fault; DSF—Deep Springs fault; ECSM—Eastern Columbus Salt Marsh fault; EF—Excelsior fault; EPF—Emigrant Peak fault; FLVF—Fish Lake Valley fault; GHF—Gumdrop Hills fault; HVF—Huntoon Valley fault; IHF—Indian Head fault; LMF—Lone Mountain fault; PSF—Petrified Springs fault; RF—Rattlesnake fault; SAF—San Andreas fault; WMF—White Mountain fault; WRF—Wassuk Range fault. These are acquired from the USGS Quaternary fault and fold database and from the Nevada Bureau of Mines and Geology (accessed July 2, 2021 at: https://www.usgs.gov/natural-hazards/earthquake-hazards/faults). The inset box in panel (b) denotes the boundary of the interferograms in Figure 2.

ages were obtained on four dates between 10 May 2020 and 17 May 2020 by two adjacent descending tracks and one ascending track (Table 1), offering three looking angles. The interferograms were processed in GAMMA (Wegnüller et al., 2016). We removed the topographic phase contribution using the 3 arcsec (∼90 m) Shuttle Radar Topography Mission (Farr & Kobrick, 2000) digital elevation model. The interferograms were filtered using a power spectrum algorithm (Goldstein & Werner, 1998), then unwrapped using the branch-cut algorithm. We georectified the interferograms to the Universal Transverse Mercator coordinate system (UTM zone 11N) with a 90 m pixel resolution (Figure 2). Lastly, we manually fixed unwrapping errors in areas that show spurious phase discontinuities and carefully removed a few patches disconnected from the main interferogram and for which the unwrapping uncertainty is high.

Table 1. Details of the InSAR imagery we used to model the 15 May 2020 MCRE (a = ascending track, d = descending track). Line-of-sight (LOS) incidence angles (from the vertical) and azimuths (degrees from N) are measured at the mainshock epicenter.

Interferogram	Track	Date 1	Date 2	LOS incidence	LOS azimuth
intf1	d144	10 May 2020	16 May 2020	33	281
intf2	d71	11 May 2020	17 May 2020	44	280
intf3	a64	10 May 2020	16 May 2020	41	80

We also collated regional GNSS coseismic offsets processed by the Nevada Geodetic Laboratory (NGL) using their updated data set released on 19 June 2020 (Blewitt et al., 2018). The data comprise continuous GNSS stations belonging to the Mobile Array of GPS for Nevada Transtension (MAGNET), Network of the Americas (NOTA), and other networks, which together provide a typical station spacing of ∼20 km across the study area (Supplementary Figure A1).

3.2 Elastic Dislocation Modeling

We solved first for the mainshock fault geometry and then for the slip distribution by jointly inverting the three unwrapped interferograms and the GNSS coseismic offsets, using a routine elastic dislocation procedure (e.g., Wright et al., 1999) described in detail below. To prepare the data for inversion, the three interferograms were downsampled using a Quadtree algorithm (e.g., Jónsson et al., 2002; Wright et al., 2003) in which the sampling block size and variance threshold were adjusted such that each downsampled dataset comprised ∼400–600 datapoints concentrated within areas of high phase gradient. We only modeled the 25 GNSS data points within the extent of the InSAR coverage, all within ∼75 km of the mainshock epicenter (Supplementary Figure A1). We experimented with using horizontal and vertical offsets or only the horizontal ones; finding little difference in our results, our final model incorporates all three components. Since the two descending interferograms share similar look angles, they are together weighted equally to the single ascending interferogram and the GNSS offset dataset.

3.2.1 Uniform Slip Modeling

We first estimated the fault location and geometry by assuming that the earthquake occurred along a rectangular fault plane in a uniform elastic half-space with Lamé constants λ and $\mu = 3.2 \times 10^{10}$ Pa. We solved the Okada (1985) equations with a downhill simplex algorithm to obtain the minimum misfit fault plane parameters (Press et al., 1992) and used 100 Monte Carlo restarts to ensure that a broad parameter space was searched (Wright et al., 1999). We solved for the minimum misfit strike, dip, rake, slip, latitude, longitude, fault length, top depth, and bottom depth. For each interferogram,

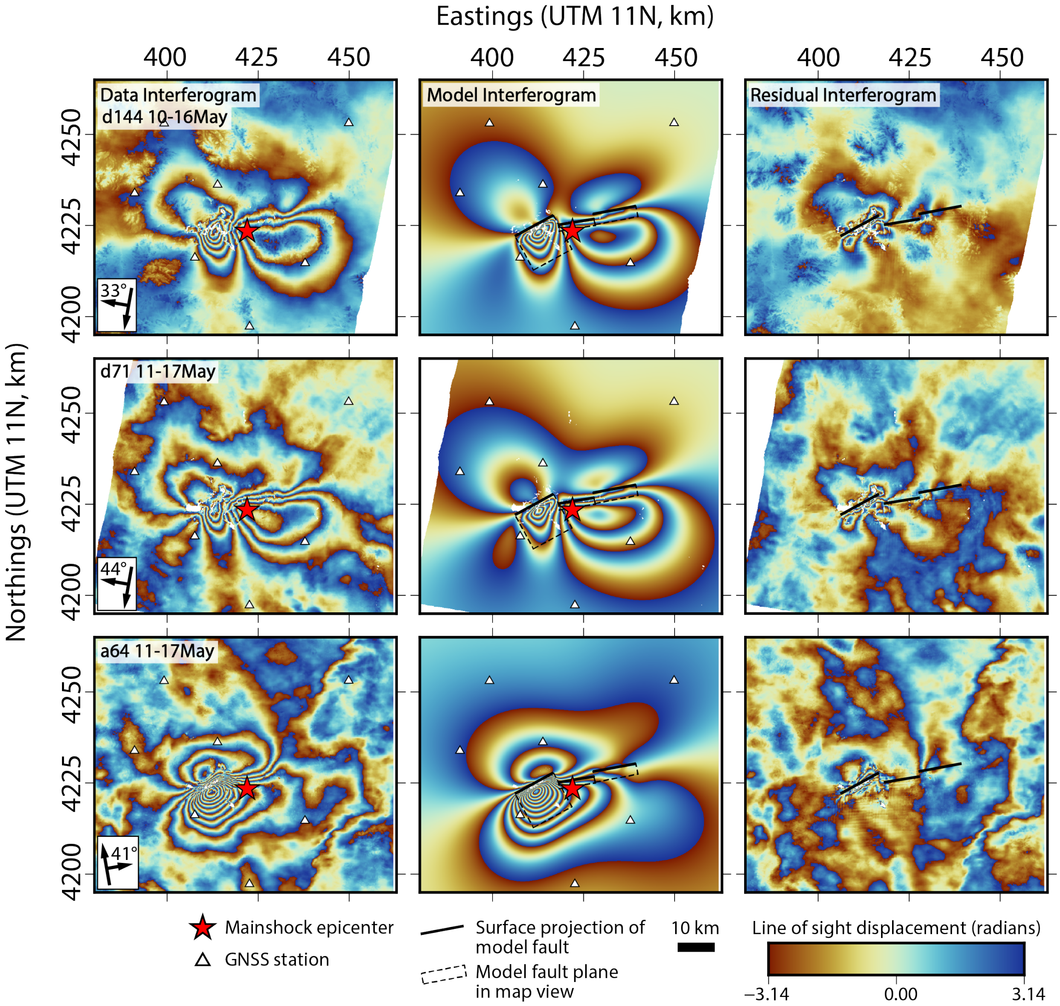

Figure 2. Observed (left column), model (middle column), and residual (right column) wrapped interferograms. The top left corner displays the satellite direction (d—descending, a—ascending), followed by the track number and the interferogram date range. The red star is the relocated mainshock epicenter, thick black lines indicate the surface projection of the model fault, the dashed box illustrates the model fault plane in map view, and long and short vectors are the satellite track and line-of-sight azimuths, respectively, with labelled incidence angles.

we also solved for 3 nuisance parameters: a translation in line-of-sight (LOS) to account for the uncertainty in LOS at the unwrapping reference point, and E-W and N-S gradients in LOS to account for residual orbital ramps.

We initially modeled the geodetic data with a single fault plane, but the resulting model interferograms did not visually fit the InSAR data well. Adding a second fault provided a much better match, accounting for the distinct fringe patterns observed west and east of the epicenter. In our final model, a third fault was added to allow for a potential change in fault geometry associated with an observed kink in the eastern fringe pattern. This three fault model provides a better visual fit and a slightly improved numerical fit compared to the simpler two fault model (Figure 2). Recognizing that the bottom depths of our model faults are poorly constrained by the geodetic data (e.g., Elliott et al., 2015), we ensured that they could not exceed 11 km, the local seismogenic thickness that we determined independently using hypocenter relocations (Section 3.3).

3.2.2 Distributed Slip Modeling

Having determined the fault geometry, we next solved for the slip distribution. We started by extending the uniform slip model fault planes along strike and up- and down-dip, to allow for the possibility of slip outside of the extents of the uniform slip model. The outer ends of the western and eastern model fault sections were extended ∼1–2 km along strike, while the bottom depths of all three sections were increased by one kilometer to 12 km to allow for tapering of slip at the base of the seismogenic zone. The extended fault planes were then each divided into 2 km × 2 km sub-fault patches, and the slip distribution was estimated using a Laplacian smoothing operator (Wright et al., 2004; Funning et al., 2005) and a slip positivity constraint (Bro & De Jong, 1997). Following Wright et al. (2004), we chose a smoothing constant that maximizes the smoothness of the slip distribution without greatly increasing the model misfit. Full parameters of our final slip model are provided in Supplementary data file C1.

3.3 Hypocentral Relocations

In addition to geodesy, we relocated the hypocenter locations of the mainshock and 196 well-recorded foreshock and aftershock events using the *mloc* multi-event relocation software (Bergman & Solomon, 1990; Walker et al., 2011; Karasözen et al., 2019; Benz, 2021). This utilizes arrival time data of multiple earthquake events recorded at multiple stations to minimize biases from unknown Earth velocity structure, and thus obtain calibrated hypocenter parameters. We used arrival time data gathered from the International Seismological Centre (ISC) bulletin and the Advanced National Seismic System (ANSS) Comprehensive Earthquake Catalog (ComCat) of the United States Geological Survey (USGS), for well-recorded events from 8 May 2020 to 3 December 2020.

Mloc adopts the hypocentroid decomposition algorithm which separates the relocation into two inverse problems, for which tailored arrival time data can be used. First, the program uses all available arrival time data at all epicentral distances to solve for the relative locations of each hypocenter in the cluster (Supplementary Figure A3). These cluster vectors connect each event to the hypocentroid—the geometric mean for all hypocenters. Second, the algorithm calculates the absolute location of the hypocentroid and updates the absolute hypocenter locations of every event in the cluster using all the arrival times at close range. In our case, more than 4,500 arrival time readings at distances of less than 0.7° contributed to the absolute relocation step (Supplementary Figures A4–5). The high density of local recordings allowed us to solve for focal depth as a free parameter, though for some events we manually adjusted depths to better fit near-source or local-distance data. We utilized a bespoke regional velocity model for the crust and upper mantle and the ak135 global model for below 120 km (Kennett et al., 1995) (Supplementary Table B1). Our relocated hypocentral data set is tabulated in Supplementary data file C2 and travel time residuals are plotted in Supplementary Figure A5.

3.4 Regional Moment Tensor Solutions

Among the 197 relocated events, we also calculated regional moment tensor (RMT) solutions for the mainshock and 89 best-recorded aftershocks. We modeled regional waveforms collected from the USGS National Earthquake Information Center (NEIC) and the Nevada Seismological Laboratory at the University of Nevada, Reno (UNR) at distances of 0–500 km. For events M_w 5.0 or smaller, we used the whole seismograms, band-pass filtered at ∼10–100 s. For events larger than M_w 5.0, we used W-phase waveforms filtered in the passband ∼50–2000 s. We solved for the RMTs by using the inversion methods, Green's functions, and central U.S. velocity model of Herrmann et al. (2011). To determine the best fit between observed and modeled waveforms, we assumed a point source and the moment tensor components were grid searched at 1 km depth intervals. The dense regional station coverage provided well-constrained centroid depths. Further sensitivity testing revealed the other RMT parameters to be insensitive to perturbations of a few kilometers in centroid depth.

3.5 UAS Survey and Field Measurements

The field observations described and discussed here are based upon the ultra high resolution (sub-centimeter/pixel) uncrewed aerial system (UAS) imagery and the detailed surface rupture mapping and fault offset measurements collected by Dee et al. (2021) and Koehler et al. (2021). We interpret these data sets in the context of our InSAR analysis of mainshock faulting (Sections 4.2, 5.1).

4 Results

4.1 Mainshock Source Model and Mechanisms

Both ascending and descending interferograms contain clear coseismic fringe patterns, with a maximum LOS displacement of ∼31 cm (away from the satellite) observed in the ascending data (Figure 2, left column). The E-W orientation of the two largest, northern and southern fringe lobes—with differing sense of LOS displacement in the ascending and descending data—is consistent with predominantly E-W, left-lateral faulting. However, there are some deviations from the general E-W trend of the central fringes, that likely represent changes in fault strike or other forms of segmentation. Furthermore, the presence of a third, more condensed southwestern lobe in the descending interferogram hints at some further complexity in the faulting mechanism. In this area, LOS of displacements are away from the satellite in both ascending and descending interferograms, consistent with localized subsidence.

Our modeling results help further illuminate the complexity in fault geometry and mechanism. Our preferred three fault model reproduces the InSAR-GNSS data well (Figure 2, central and right columns, and Figure S1), with a root mean square residual displacement of ∼0.9 cm. The three model faults are each 10–12 km long, and are aligned roughly end-on-end for a total length of ∼34 km (Table 2). None of the model faults align with previously mapped structures. The eastern and central faults strike 79.4° and 80.8°, respectively, and are separated by a ∼1.4 km left step in the surface trace. The western fault strikes more northerly at 61.5°, in agreement with the observations. The eastern and central faults dip steeply southwards at 75.8° and 81.6°, respectively, while the western fault dips more gently at 48.4° SE. The western fault also has a distinct mechanism. Whereas the eastern and western faults are predominantly left-lateral (rake −4.4° and 0.0°, respectively), the western fault exhibits oblique normal-sinistral motion (rake −47.5°). This explains the subsidence observed in the southwestern lobe of the descending interferogram discussed earlier.

Overall, slip extends to 12 km depth on each model fault (Figure 3), the maximum allowed on the basis of the local seismogenic thickness (Section 3.2.1). The gentler dip of the western model fault gives it the greatest fault width and the largest rupture area. However, of the total geodetic moment of 5.8×10^{18} Nm, ∼40% occurs on the central model fault and ∼30% each on the western and eastern faults. Maximum slip of 1.1 m occurs on the central fault plane at 8–10 km depth; peak slip on the eastern fault of 0.9 m occurs at a similar depth, but peak slip on the western fault of 0.9 m is much shallower at ∼1.5–3.0 km. All three model faults exhibit a clear shallow slip deficit. This is most pronounced along the central and eastern faults, and somewhat less so along the west-

Table 2. Parameters of our preferred three fault InSAR-GNSS distributed slip model. Easting and Northing refer to the center coordinates of the model fault surface projection. The peak slip depth refers to the central depth of the peak slip sub-fault patch. The full slip distribution is tabulated in Supplementary Table S2.

Model fault	**Easting (km)**	**Northing (km)**	**Strike (°)**	**Dip (°)**	**Rake (°)**	**Length (km)**	**Width (km)**	**Bottom depth (km)**	**Moment ($\times 10^{18}$ Nm)**	**Peak slip (m)**	**Peak slip depth (km)**
Western	411.428	4224.957	61.5	48.4	-47.5	12.0	16.0	12.0	1.9	0.9	2.2
Central	423.000	4226.000	80.8	81.6	0.0	10.0	12.0	11.9	2.4	1.1	8.9
Eastern	433.491	4229.243	79.4	75.8	-4.4	12.0	12.0	11.6	1.5	0.9	8.7

ern fault, where up to 0.2 m of model slip reaches the shallowest sub-faults. We discuss these points further in Section 5.4.

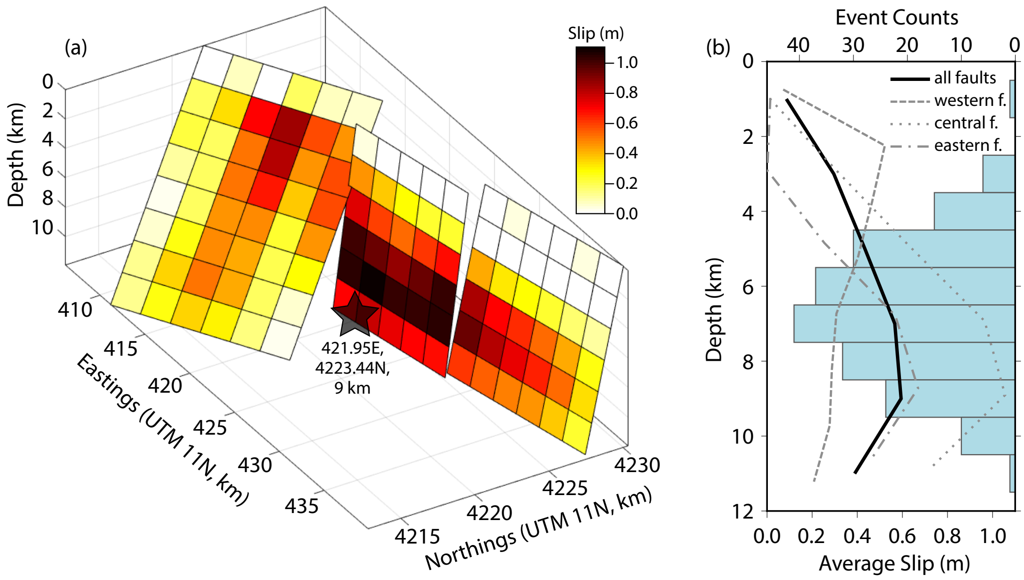

Figure 3. (a) 3D view of our preferred InSAR-GNSS distributed slip model. Each sub-fault patch is 2 km×2 km and the star shows our relocated mainshock hypocenter. Full parameters of each sub-fault patch are tabulated in Supplementary data file C1. (b) Model slip and aftershock depth profiles. Dashed and dotted gray lines show the average slip for each of the three model faults, plotted against the central depth of each row of sub-faults. The thick black line shows the weighted average for all three model faults, calculated by averaging all sub-fault patches within 2 km depth increments and plotting against the central depth of the bin range. The histogram shows the number of calibrated relocated earthquakes at each 1 km increment in focal depth.

Our seismological analyses reveal additional characteristics of the mainshock rupture. The relocated, calibrated mainshock hypocenter is located deep (9 km) on the central model fault plane, close to the peak model slip (Figure 3a), indicating that the earthquake ruptured bilaterally and mostly up dip. The W-phase moment tensor is predominantly strike-slip but exhibits a significant non-double couple component, and is broadly consistent with the orientation and kinematics of our InSAR fault model (Figure 4a). The W-phase centroid depth of 11 km is a little below the peak slip depth in our InSAR model of 8–10 km (Supplementary Figure A2, Table C3), and the W-phase moment of 6.8×10^{18} Nm is a little larger than the geodetic moment.

4.2 Mainshock Surface Ruptures

Field observations include faults with discernible slip and measurable offset, and smaller cracks without clear kinematic indicators (Dee et al., 2021; Koehler et al., 2021). These features have a variety of orientations and are broadly distributed without consistent alignment along a single through-going fault (Figure 5a, 6). In the central and eastern part of the rupture area, field observations of surface deformation are sparse, and mostly located off the main faulting as revealed by InSAR. This is consistent with our InSAR modeling, which shows a pronounced shallow slip deficit in this area. The longest alignment of surface ruptures is immediately south of and conjugate to the central model

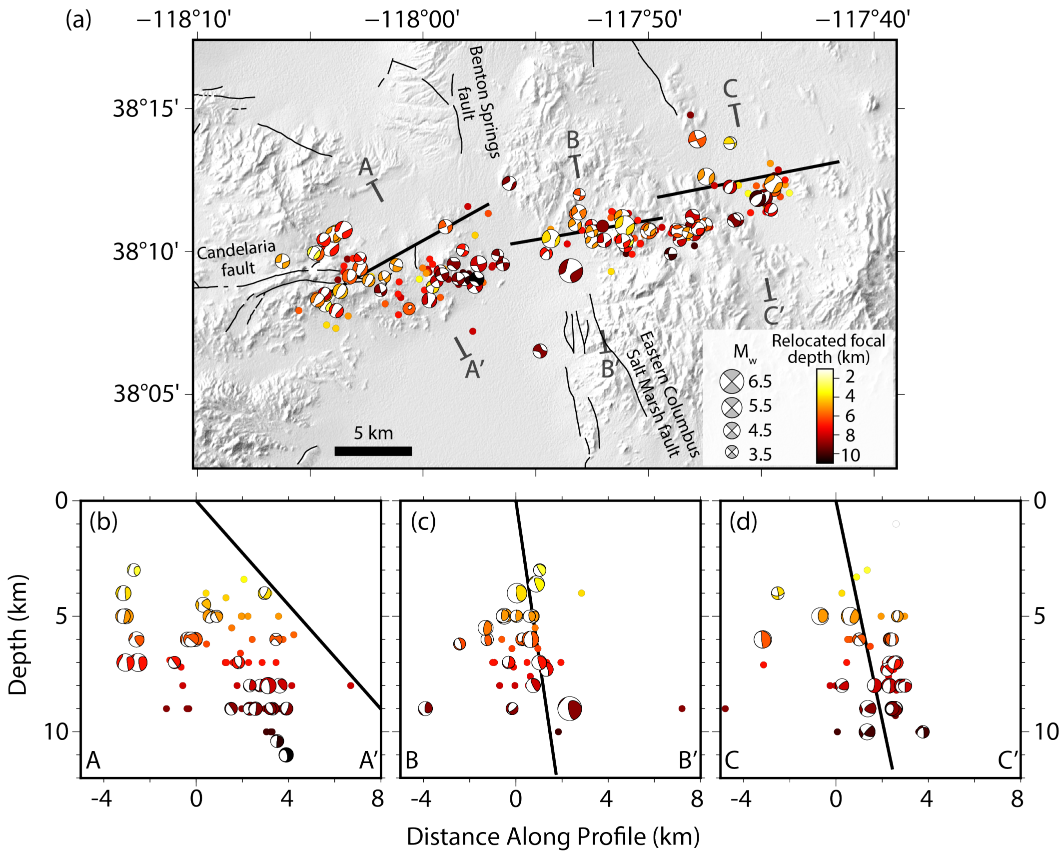

Figure 4. (a) Multi-directional hillshade map showing the relocated hypocenters and their focal mechanisms where available, plotted and colored by calibrated focal depth. Focal mechanisms are lower hemisphere projections scaled by moment magnitude. Smaller circles are events that are too small for waveform modeling (M_w<3.5) plotted without any magnitude scaling. The thick black lines indicate the surface projection of the three model faults, and thin black lines are the US Quaternary faults (see Figure 1 for details). The black T-shape lines denote the cross-section transects. (b–d) Cross-sectional views of the relocated hypocenters and focal mechanisms, plotted and colored by calibrated focal depth. Earthquakes are included where they lie within 5 km (c) or 6 km (b, d) of the cross-section lines on (a). Focal mechanisms are back-hemisphere projections scaled by moment magnitude and, similar to (a), smaller circles are the remaining relocated hypocenters without mechanisms. Thick black lines are cross sections of the (b) western, (c) central and (d) eastern model faults.

fault (Figure 6b,c), and involves up to ∼10 cm of right-lateral motion over a distance of ∼2 km (Dee et al., 2021; Koehler et al., 2021).

Most of the observed surface faults and cracks lie within the western part of the mainshock fault zone and are the main focus of this section. There are two main alignments of fractures, both trending approximately northeast (Figure 5b,c). The first, narrower alignment approximates the trace of the western model fault over a distance of ∼10 km, and accommodates up to ∼10 cm of left-lateral and ∼7 cm of vertical motion. These motions are roughly consistent with our InSAR analysis, which supports up to ∼20 cm of surficial, oblique (normal-sinistral) slip along the SE-dipping, western model fault. However, the vertical slip observed in the field exhibits a mix of down-to-the-southeast (DTSE) and down-to-the-northwest (DTNW) throw (Figure 6a), indicating that the shallow faulting is more complex than our InSAR model can resolve.

The second main alignment of fractures lies ∼1–3 km to the northwest of and subparallel to the first alignment, and contains the largest slip observed anywhere in the field (Figure 5b,c). This comprises several discrete arrays of faults and cracks, distributed even more diffusely than in other areas, with thousands of individual fractures across a ∼6 km by ∼1 km zone. Though the overall trend is northeastwards, individual fracture sets exhibit a wide variety of orientations. Where fault slip can be resolved, the kinematics are predominantly left-lateral (with offsets of up to ∼20 cm) and vertical, DTNW (with throw of up to ∼10 cm). Though this fracture zone does not align with our InSAR model faults, it is consistent with a minor discontinuity visible in the unwrapped interferograms (Figure 7a). The sense of the LOS displacement discontinuity in the ascending interferogram supports that the left-lateral motion dominates over the vertical component across this second fracture alignment.

Many of the fractures also exhibit a clearing of loose pebbles or gravel from only one side of each crack (Figure 6). This phenomenon is particularly evident where fractures break desert pavement surfaces, and is generally absent from sandy surfaces. The width of the cleared zone is typically a few centimeters, large enough that the cleared side could be mapped from fine-resolution UAS imagery (Dee et al., 2021; Koehler et al., 2021). The side that is cleared is consistent within each fracture set but can vary between sets. For example, fractures along the second, northwestern alignment are predominantly cleared of pebbles to the southeast (upthrown) side (indicated by the tip of white triangles in Figure 7a). Only a few are bilaterally cleared. We interpret that the predominance of unilateral clearing may represent significantly higher ground acceleration on one side of each fracture during the rupture process, perhaps related to local rupture dynamics. We further discuss the importance of these fractures in Section 5.1.

4.3 Aftershocks Distribution and Mechanisms

The relocated aftershock hypocenters are scattered along a ∼35 km-long, ∼ENE trend, and span a focal depth range of 1–11 km with a concentration at ∼4–9 km (Figure 4). Individual hypocenters have typical, formal uncertainties of ∼0.4–0.6 km in epicentral coordinates (the average lengths of the short and long semi-axes of the 90% confidence ellipse) and estimated uncertainties of ±1–4 km in focal depth. RMT centroid depths are generally in close agreement (Supplementary Figure A2), but extend to slightly deeper depths of 15 km. We conservatively estimated centroid depth uncertainties to be ∼5 km, so we do not view the differences with focal depths to be significant. However, we consider the focal depths most reliable on the basis of their smaller depth uncertainties and overall narrower depth range.

The relocated aftershocks approximate the trend of the InSAR model faults, although on close inspection they are concentrated mostly to the south of the fault surface projections. This is especially evident for the western model fault, where aftershocks reach as far as ∼4–5 km southeast of its surface trace. The overall aftershock distribu-

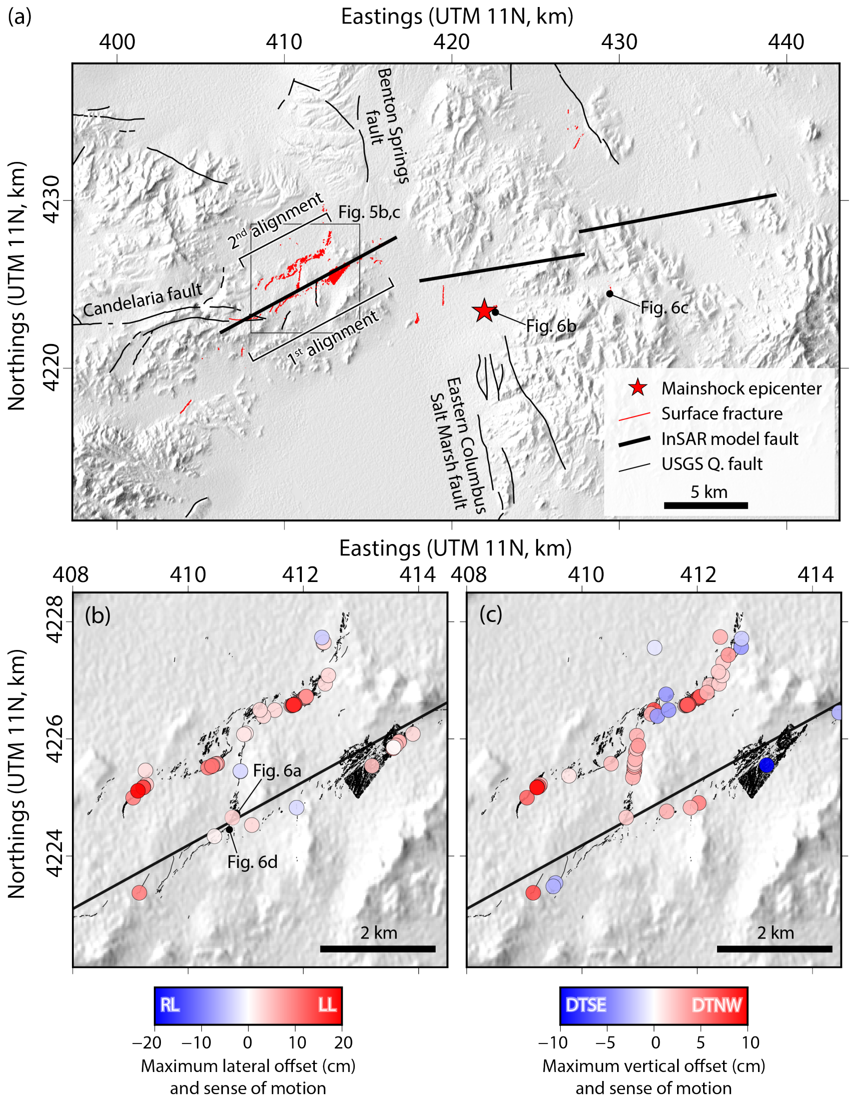

Figure 5. (a) Multi-directional hillshade map showing our calibrated relocated MCRE mainshock epicenter (red star), MCRE surface faulting and cracks mapped in the field (Dee et al., 2021; Koehler et al., 2021) (thin red lines), surface projections of our InSAR-GNSS model faults (thick black lines), and regional active faults as in previous figures (thin black lines). The inset box indicates the extent of panels (b) and (c). (b) Lateral and (c) vertical fault offsets measured in the field. Where several measurements were collected from the same locality, we take the maximum. The red- and blue-shaded circles represent the sense of motion, with the color gradient reflecting the amount of fault offset in centimeters. Positive values are assigned to left-lateral offsets in (b) and down-to-the-NW (DTNW) offsets in (c). Thin black lines are the near-field fractures, and the thick black line is the surface projection of the western model fault.

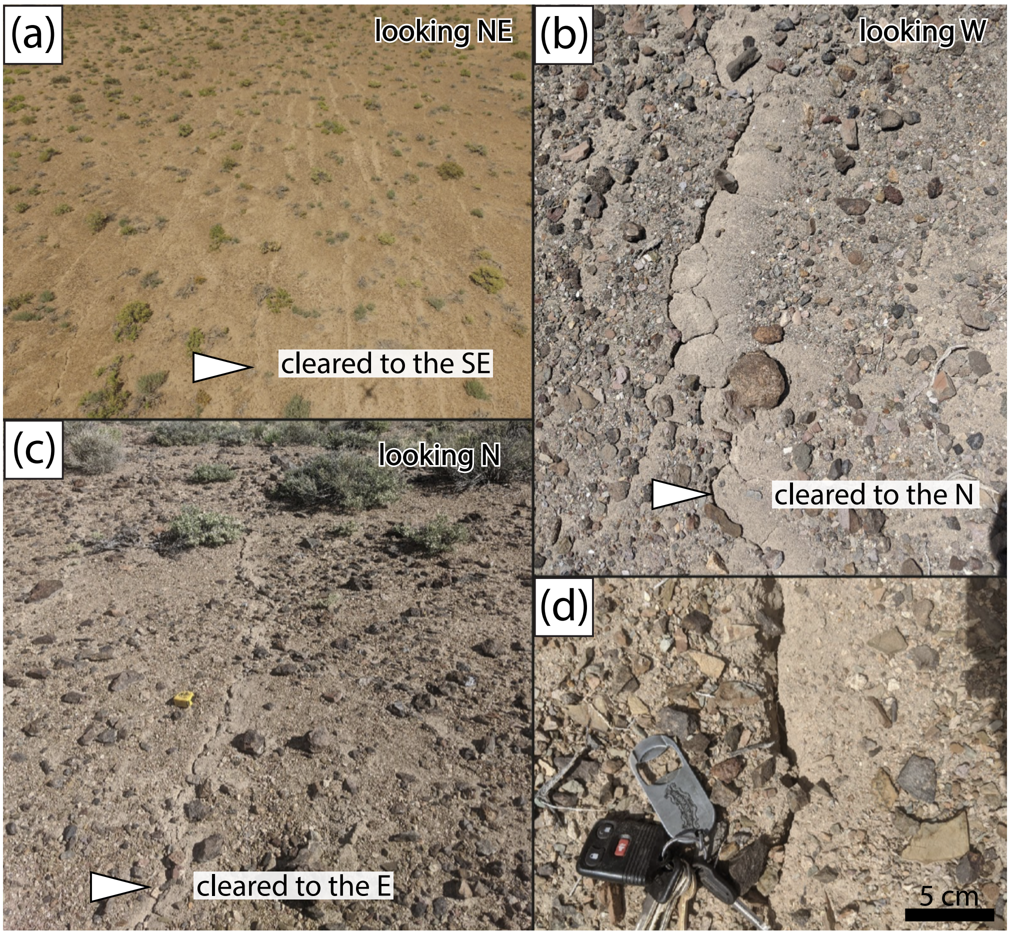

Figure 6. Photos of cleared crack phenomena from locations indicated in Figure 5a–b. (a) Oblique UAS view looking northeast of a crack field with clearings on the right (southeast) side of each crack. (b) Photo looking west, with a crack cleared to the north. (c) Photo looking north, with a crack cleared to the east (tape measure for scale). (d) Close-up of crack showing clearing of loose materials on one side of the crack. Tips of the white triangles point to the direction of cleared pebbles, similar to the symbology used in Figure 7. Geographic coordinates of a–d are as follows: (38.1657, −118.0184), (38.1562, −117.8840), (38.1658, −117.8060), (38.1641, −118.0190).

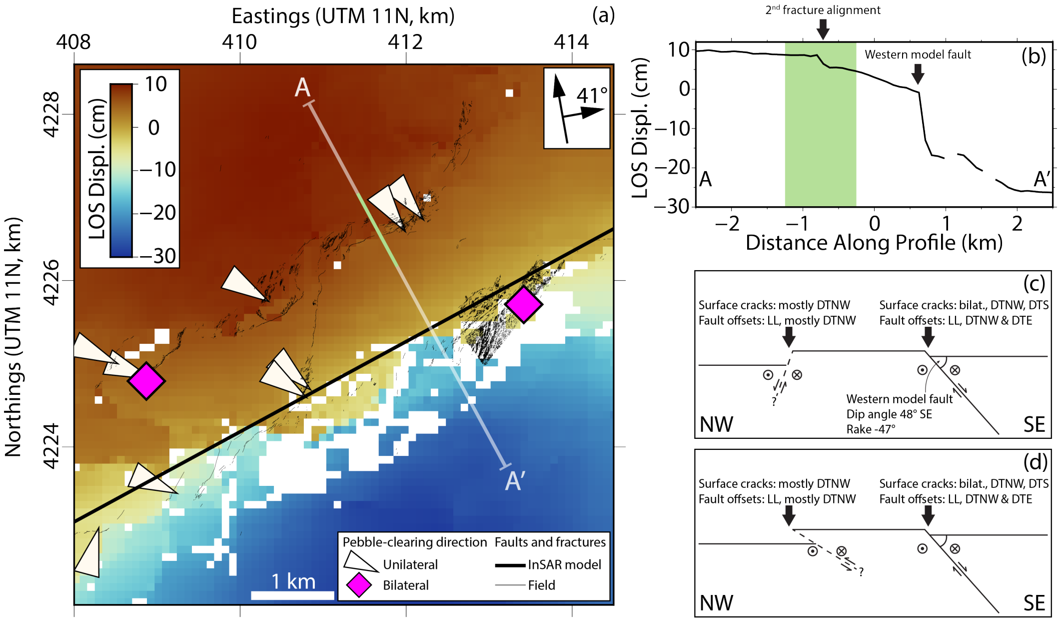

Figure 7. (a) Unwrapped ascending interferogram of the western MCRE rupture area showing the LOS displacement jump along the surface projection of the western model fault (thick black line). Thin black lines indicate fault offsets and cracks mapped in the field (Dee et al., 2021; Koehler et al., 2021). The white triangles and magenta diamonds represent the location of fracture sets that exhibit unilateral and bilateral pebble clearings, respectively. Triangle tips point to the cleared pebble side or upthrown direction of the fracture. (b) Transect of unwrapped LOS displacements along A–A' in panel (a). The shaded area illustrates a secondary LOS displacement discontinuity which co-locates with the second fracture alignment. (c,d) Two, competing, interpreted cross-sections of the fault structure and kinematics in the western MCRE, derived from combining near- and far-field observations. The SE-dipping solid black line is the InSAR western model fault. Dashed black lines are the interpreted (c) NW-dipping normal-sinistral and (d) SE-dipping reverse-sinistral oblique faults beneath the second fracture sets with DTNW sense of throw. Abbreviations: bilat—bilateral; DTE—down-to-the-east; DTNW—down-to-the-northwest; DTS—down-to-the-south; LL—left-lateral.

tion therefore supports the SE-dipping fault geometry inferred from InSAR modeling. However, both the map distribution of aftershocks (Figure 4a) and cross-sections (Figure 4b–d) also reveal numerous off-fault events up to several kilometers from the mainshock model faulting. One cluster of off-fault aftershocks is located at the western end of the western model fault, but no equivalent cluster of aftershocks at the eastern end of the mainshock rupture is present. Other clusters are distributed along ∼NW-SE trends, conjugate to the mainshock faulting.

The aftershock RMTs exhibit a mix of strike-slip and normal mechanisms, many of them with ENE-trending nodal planes (Figure 4a). In the central and eastern rupture area, most aftershock mechanisms are predominantly strike-slip with ENE-trending sinistral nodal planes, and therefore roughly consistent with our InSAR model. However, based on the presence of conjugate trends in relocated epicenters and field observations of scattered dextral offsets in this region, we interpret that some of these aftershocks involve NNW-striking right-lateral faults. We also observe many aftershocks with pronounced non-double couple components. Like the mainshock, these smaller aftershocks may have involved multiple faults of differing kinematics, summing to a non-double couple mechanism.

In the western part of the rupture area, there is a wider mix of aftershock mechanisms including pure normal, oblique-normal, and strike-slip faulting. The normal mechanisms are concentrated near the western end of the rupture, are relatively shallow, and mostly involve NE-trending nodal planes slightly oblique to the western model fault. The strike-slip mechanisms are concentrated near the eastern half of the western model fault, are relatively deep, and have ENE-trending, sinistral nodal planes. This hints that our western InSAR model fault is an oversimplification, with the real faulting at depth involving distinct strike-slip and normal faults that are in close proximity but slightly oblique to one another.

4.4 Comparisons with other Geodetic Slip Models and Seismological Observations

We now compare our mainshock slip model with four other previously published models: Cui et al. (2021) and S. Li et al. (2021) who like us inverted InSAR and GNSS displacements to solve for fault geometry and slip distribution, and Zheng et al. (2020) and Liu et al. (2021) who also incorporated a range of seismological data to solve for the kinematic rupture process. While we also acknowledge the GNSS-derived uniform slip model of Hammond et al. (2021), this lacks the spatial resolution of the InSAR-based models and is excluded from our comparison.

Though the source geometries vary in detail between the five studies, all models including ours exhibit comparable kinematics: almost pure sinistral slip on steep SSE-dipping faulting in the east and oblique normal-sinistral slip on a more gently SE-dipping structure in the west. In the east, ours is the only model that subdivides the sinistral fault into two discrete sections, to account for any potential changes in fault geometry associated with a bend in the observed InSAR fringes (Figure 2, left column). Though our model reduces the misfit in this area, we acknowledge that there is little change in fault geometry or kinematics across this model subdivision, and so we are hesitant to characterize it as real fault segmentation. Our dip values of 76–82° for these model faults are consistent with three of the other studies (78–83°) but steeper than the dip obtained by Cui et al. (2021) of 65°.

In the west, our single oblique western model fault is similar to that of Zheng et al. (2020), Cui et al. (2021), and S. Li et al. (2021), and only Liu et al. (2021) subdivide this section into two sub-faults, one dipping steeply below ∼5 km and one dipping gently above. Our model fault dip of 48° is intermediate between the other models (40–64°). However, as described in Section 4.3, our aftershock relocations and mechanisms suggest that all of these mainshock models are oversimplified. The aftershock data support a NE-striking normal fault and an ENE-striking left-lateral fault in this area, with our western model fault effectively averaging the two in location, strike, and rake. This highlights the limitations in spatial resolution of geodetic slip modeling and the importance of incorporating complementary aftershock data sets to illuminate the mainshock rupture in greater detail. Similarly, none of the InSAR models (including our own) capture the ∼6 km-long fracture system that we have observed 1–3 km northwest of our western model fault. Again, this goes to show an important limitation in the spatial resolution of InSAR slip models.

Where our model differs most significantly from the other three published models is in the depth extents of the coseismic slip. Whereas the bottom depth of our slip model is limited to 12 km on the basis of calibrated focal depths, the other models have no such constraint and include slip to depths of ∼15–20 km (Zheng et al., 2020; Cui et al., 2021; S. Li et al., 2021; Liu et al., 2021) (Figure 8), even though slip below ∼10 km is in fact poorly resolved by available geodetic data, as acknowledged by Liu et al. (2021) in their checkerboard resolution test. The bottom depth of these models is several kilometers below the deepest calibrated aftershock at 11 km ±1–4 km (Section 4.3), which we take to indicate the local seismogenic thickness. Our shallower bottom depth likely explains why our model moment of 5.8×10^{18} Nm is 15–25% smaller than that of Zheng et al. (2020) and Liu et al. (2021). This provides another example of how carefully calibrated aftershock data are useful in constraining mainshock properties.

There are also some more subtle differences in the slip distribution and peak slip depth between the four models. All five models show slip concentrated in two areas; a shallow (<5 km) slip asperity on the western, oblique fault, and a deeper (>5 km) asperity on the main sinistral fault in the east. Zheng et al. (2020), Cui et al. (2021), and S. Li et al. (2021) place peak slip on the western fault at ∼3–5 km depth, whereas we and Liu et al. (2021) place peak slip on the eastern fault at ∼6–10 km depth (Figure 3b). Our peak slip of 1.1 m lies within the range of 0.6–1.7 m of the other four models. All five models display a pronounced shallow slip deficit (Figure 8), but whereas we have up to ∼0.2 m of surface slip on the western fault (in agreement with field observations), Liu et al. (2021) only have surface slip in the east where our model has almost none. Cui et al. (2021) have up to 0.4 m of shallow surface slip on both their model faults; Zheng et al. (2020) and S. Li et al. (2021) have none on either fault. We return to the shallow slip deficit in Section 5.4.

Lastly, we compare our seismological results with those from Ruhl et al. (2021) which also incorporated eight temporary seismic stations deployed soon after the mainshock (Bormann et al., 2021). They located and then relocated (with waveform-based double-differencing) ∼18,000 events from January 1 to August 31, 2020, and used regional waveform modeling to estimate 128 moment tensors including for the mainshock. For the mainshock, their double-difference based depth is 3.7 km but their waveform model is 8.0 km, consistent with our InSAR peak slip at 8–10 km and within error of our own W-phase centroid depth of 11 km. Their best double-couple approximation of the fault plane shares the same strike and agrees to within 7° in dip and rake with ours. However, their mechanism has a higher double-couple percentage (>95% versus ∼68%). Their relocated aftershocks are distributed almost exclusively above 12 km, in close agreement with our arrival time-based calibrated focal depth range (up to 11 km) and a little shallower than our RMT centroid depth range (up to 15 km). Their aftershock moment tensors include a wide variety of strike-slip and normal mechanisms, similar to ours. Their aftershock results are not tabulated so we cannot compare event-to-event locations or moment tensors.

In cross-sectional view, the denser, double-difference relocated aftershock clouds of Ruhl et al. (2021) exhibit clear alignments that are not apparent in our own sparser data. These include structures that appear to align with our InSAR model faults. For

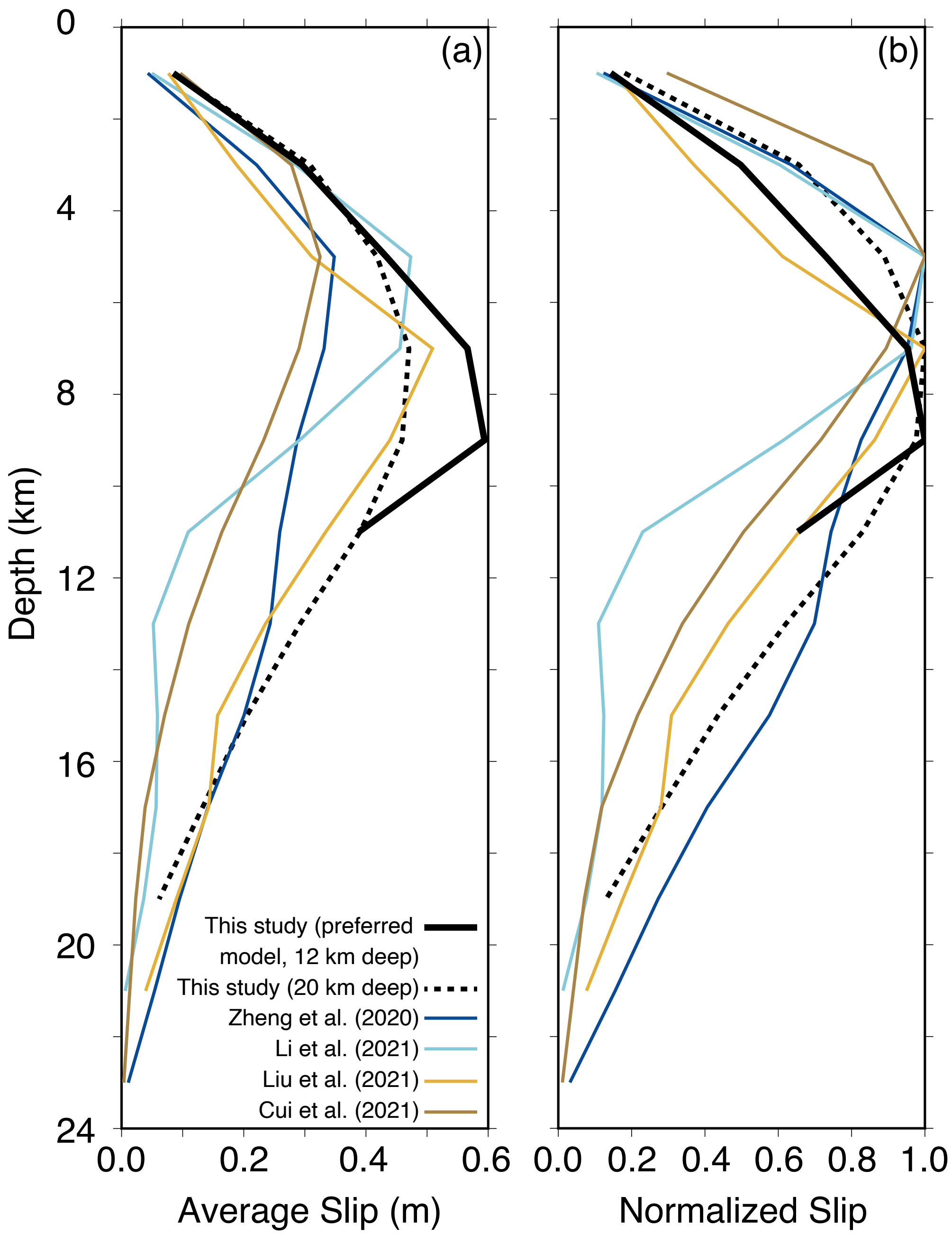

Figure 8. Comparison of MCRE geodetic model slip profiles from our paper and other studies. (a) Average and (b) normalized slip in 2 km depth increments, demonstrating the pronounced shallow slip deficit. See Section 5.4 for details of the slip profile calculations and further discussion.

example, a transect across the central rupture zone reveals distinct shallow, ∼60°-dipping and deep, sub-vertical structures (Figure 5e in Ruhl et al., 2021), consistent with the geometry of mainshock slip at the intersection of our western and central InSAR model faults (Figure 3a).

5 Discussion

5.1 Kinematics of the Mina Deflection

The mix of sinistral and sinistral-normal faulting in the MCRE and its aftershock sequence is consistent with the kinematics of the surrounding active faults in the Mina deflection, in particular the well-studied, neighboring Candelaria fault which exhibits both vertical scarps and sinistral geomorphic offsets (Wesnousky, 2005) (Figures 4, 5). The off-fault aftershock cluster at the western end of our model fault might be associated with energy radiated at the western rupture termination, reactivating the Candelaria and other local faults. We interpret that NW-striking dextral faults are also involved in the MCRE sequence. Focal mechanisms conjugate to the central and eastern model faults project along strike with the major right-lateral Benton Springs and Petrified Springs faults, which help accommodate dextral shear transferred through the Mina deflection (Figure 1) (Wesnousky, 2005; DeLano et al., 2019). The overall kinematics, however, are consistent with the block rotation model for dextral slip transfer (Wesnousky, 2005), while also supporting a component of transtension on some of the faults (e.g., Oldow, 2003). The E-striking, sub-vertical, sinistral mainshock faults in the east of the rupture zone presumably rotate clockwise about vertical axes in order to accommodate regional dextral shear, while the NE-trending western fault involves transtension. Normal faulting aftershock focal mechanisms located at the ends of the mainshock faulting also support the paired basins produced as a result of block rotation (Wesnousky, 2005). In the long-term, these block rotations may divert fault orientations away from those favorable to slip, promoting the formation of new faults and preventing older ones from becoming structurally mature. We discuss this point further in Section 5.3.

Our combination of far- and near-field surface deformation observations reveals the kinematics of the western MCRE faulting in particular detail. Our western InSAR model fault exhibits normal-sinistral oblique-slip, dips to the SE, and the unwrapped data interferogram shows a clear LOS displacement jump of 12 $\pm$4 cm (Figure 7a,b). Approximately 1 km to the northwest and sub-parallel to the model fault, the InSAR signal displays a more subtle change in LOS displacement of 2 $\pm$1 cm across a 100–150 m distance. Along the same trend, our field measurements show distributed faults and surface cracks with pebble-clearing features (Figure 6). The fault offsets are dominantly left-lateral—consistent with the sense of LOS change in the raw interferograms—and DTNW (Figure 5b,c). The preferential clearing of pebbles to the southeast also implies that the southeast side is up and northwest side is down (Figure 7a, white triangles). This is opposite to that of the main fault, suggesting an upthrown block in between two, sub-parallel faults.

We propose two, competing structural models to explain these observations. In the first model, the secondary fault structure controlling the fracture alignment dips to the NW and away from the main fault, accommodates normal-sinistral slip, and forms a horst structure (Figure 7c). However, the absence of normal-faulting aftershocks to the northwest and along strike of the putative NW-dipping oblique fault implies that this may only be a very shallow structure (Figure 4a). In the second model, the secondary fault structure dips to the SE, sub-parallel to the main fault, and slips in a reverse-sinistral sense (Figure 7d). Contrastingly, although the distributed aftershocks in the footwall block of the western model fault may imply a SE-dipping structure, we do not observe any reverse focal mechanisms (Figure 4b).

5.2 Implications for Earthquake and Seismic Hazard Characterization in Regions of Highly-distributed Faulting

Along the secondary structure, our InSAR, field, and seismological observations are only in agreement to a certain degree. The discrepancies reflect each method's strengths and resolution in light of the geological complexity of the area. The poor depth resolvability of the shallowest aftershocks ($\sim$<4 km) illustrate the limitations of using regional seismograms to characterize the shallowest structures, but aftershock relocations and mechanisms offer unique constraints on fault complexity within the deeper seismogenic layer. The shallower structures are likely best represented by field observations, while InSAR—despite its high coherence due to the ideal desert conditions of this region—may better capture the mainshock rupture at larger length- and depth-scales.

Our study therefore highlights the care needed for earthquake characterization and seismic hazard assessment in regions of highly-distributed faulting. The integration of geodesy, seismology, and field geology, perhaps along with other methods, is required to resolve the complexity of a large earthquake sequence along and across strike and down dip. A single method, on its own, could easily lead to misinterpretation. For seismic hazard assessment, simple fault length-magnitude scaling relations would not have anticipated an earthquake of the magnitude of the MCRE, and the characteristic earthquake model is probably inapplicable in a region of such diffuse faulting. Furthermore, paleoseismic trenching would likely be required across a very large number faults for the full history of major earthquakes in this region to be captured, but could still miss large events that did not rupture fully to the surface.

5.3 Evidence of Structural Immaturity in the MCRE

The MCRE exhibits several characteristics that may reflect the structural immaturity of the fault system. Firstly, the mainshock geometry is rather complex for an earthquake of this magnitude, with two distinct kinematic styles: sub-vertical left-lateral faulting in the east and inclined, normal-sinistral faulting in the west. The short segmentation length scale of $\sim$10 km presumably reflects the shallow thickness of the seismogenic zone as revealed by our aftershock depths (Klinger, 2010). The fracture systems located away from the main fault trace reflect non-localized deformation commonly observed in immature fault zones (e.g., Zinke et al., 2015). The off-fault distribution of aftershocks, their non-double couple focal mechanisms, and their wide variety of kinematics and orientations (Figure 4) are further indications of a lack of a dominant through-going structure in the area. In addition, Liu et al. (2021) reported an average mainshock rupture velocity of $\sim$1.5 km/s, a relatively slow speed that is in agreement with other earthquakes along immature faults (e.g., Perrin et al., 2016; Chounet et al., 2018).

Finally, there is a limited expression of clear, neotectonic landforms along the mainshock fault trace such as scarps, channel offsets, or shutter ridges (Figure 9). As revealed by InSAR, the main fault trace of the MCRE trends approximately along strike from the Candelaria fault (Figure 1), which itself exhibits net, sinistral-normal slip of $\sim$900 m since $\sim$3 Ma (Wesnousky, 2005). We attempted to quantify the cumulative offset along the MCRE rupture using Sentinel-2B multi-spectral imagery and digital topography (Figure 9). Despite a rich and varied surface geology, we found only two potential long-term slip indicators: an outcrop comprising sedimentary rocks of the Candelaria (Triassic) and Palmetto (Ordovician) formations (Figure 9g,h) (Ferguson et al., 1954) and a ridge of Pliocene andesite (Figure 9i,j) (Ferguson et al., 1953), both showing apparent sinistral offsets of $\sim$600–700 m and $\sim$200 m, respectively. However, we are not confident that these are true markers of net slip. Elsewhere, the limited development of discernible long-term geomorphic faulting along the remaining $\sim$30 km-long rupture indicates that the causative fault has not yet accumulated offset that is resolvable from satellite imagery. In addition, where known, the E-trending sinistral faults in the Mina deflection have slow slip rates of ∼0.3–0.4 mm/yr (Speed & Cogbill, 1979; Lee et al., 2006), and the rates of the unmapped faults of the MCRE may be slower still—another mark of structural immaturity. The weak manifestation of geomorphic features likely reflects that crustal block rotations produce diffuse, highly segmented faulting rather than a long, through-going fault. With all of these characteristics, we interpret that the MCRE provides an example of rupture along a fault of pronounced structural immaturity.

5.4 Shallow Slip Deficit in the MCRE

Averaged over several earthquake cycles, the offset accommodated across a fault zone should be constant with depth. However, geodetic slip inversions of large earthquakes commonly exhibit peak model slip at depths of ∼3–6 km with a reduction closer to the surface, termed the shallow slip deficit (e.g., Simons et al., 2002; Fialko et al., 2005). The effect is often illustrated with a normalized slip profile (a plot of average slip against depth normalized against peak average slip) and parameterized as one minus the normalized slip of the surficial row of model slip patches (usually expressed as a percentage). While absolute values depend in part upon whether or not near-field geodetic data are incorporated (Vallage et al., 2015; Xu et al., 2016; Marchandon et al., 2018; C. Scott et al., 2019), upon the assumed elastic structure (Amoruso et al., 2004; Hearn & Bürgmann, 2005; Barbot et al., 2008; Marchandon et al., 2021), and upon other choices made in the modeling (Huang et al., 2017; Ragon et al., 2018; Y. Li et al., 2020), the general inference of shallow slip deficit in many large earthquakes is considered robust. Moreover, SSDs are also manifest in field measurements of surface slip along the primary fault trace (Dolan & Haravitch, 2014).

Several possible mechanisms causing SSD have been invoked, each with important implications for fault mechanics and earthquake physics. A switch to velocity-strengthening fault friction at shallow depths would naturally favour aseismic over seismic slip (C. J. Marone et al., 1991; C. Marone, 1998). Damaged zones above a strike-slip fault may have a locally reduced seismic velocity, promoting inelastic off-fault deformation (Zhang et al., 2009). Regions surrounding the shallow fault might undergo distributed deformation predominantly during the interseismic period, thereby accumulating little elastic strain (Fialko et al., 2005; Lindsey et al., 2014). Coseismic rupture might dissipate in the near surface through plastic yielding, particularly when near-surface materials are poorly-consolidated (Kaneko & Fialko, 2011; Brooks et al., 2017; Roten et al., 2017). Alternatively, SSDs might simply reflect random differences in the depth extents of individual ruptures within the seismogenic zone (Berberian et al., 2001; H. Yang & Yao, 2021; Yao & Yang, 2022). This would help explain why the largest events (M_w>7.5), which are those most likely to fill the entire seismogenic layer and drive slip in any velocity strengthening region, generally have reduced or absent SSDs (Tong et al., 2010; Lauer et al., 2020). Finally, SSDs might arise due to assumptions made in geodetic slip models, such as simplification of the Earth's elastic structure (Xu et al., 2016), or due to near-fault image decorrelation leading to insufficient surface displacement data points to solve for shallow slip (Fialko et al., 2005).

Understanding what causes SSDs and how they might be compensated is vital for seismic hazard assessment, for a number of reasons. Firstly, active fault mapping, slip rate estimations, and paleoseismic trenching all rely upon surface offsets. As such, a pronounced SSD decreases confidence in the link between surficial geological measurements and earthquake faulting at depth (Dolan & Haravitch, 2014; Brooks et al., 2017). Secondly, the suppression of near surface slip can affect strong ground motions near the fault trace (Kaneko et al., 2008; Pitarka et al., 2009). Thirdly, there is the possibility that the slip deficit is removed by subsequent earthquakes centered at shallower depths (Berberian et al., 2001; Jackson et al., 2006; Elliott et al., 2011; Mackenzie et al., 2016). Alternatively, shortfalls in coseismic surface slip could be compensated through distributed coseismic deformation away from the main fault trace (Rockwell et al., 2002; Simons et al.,

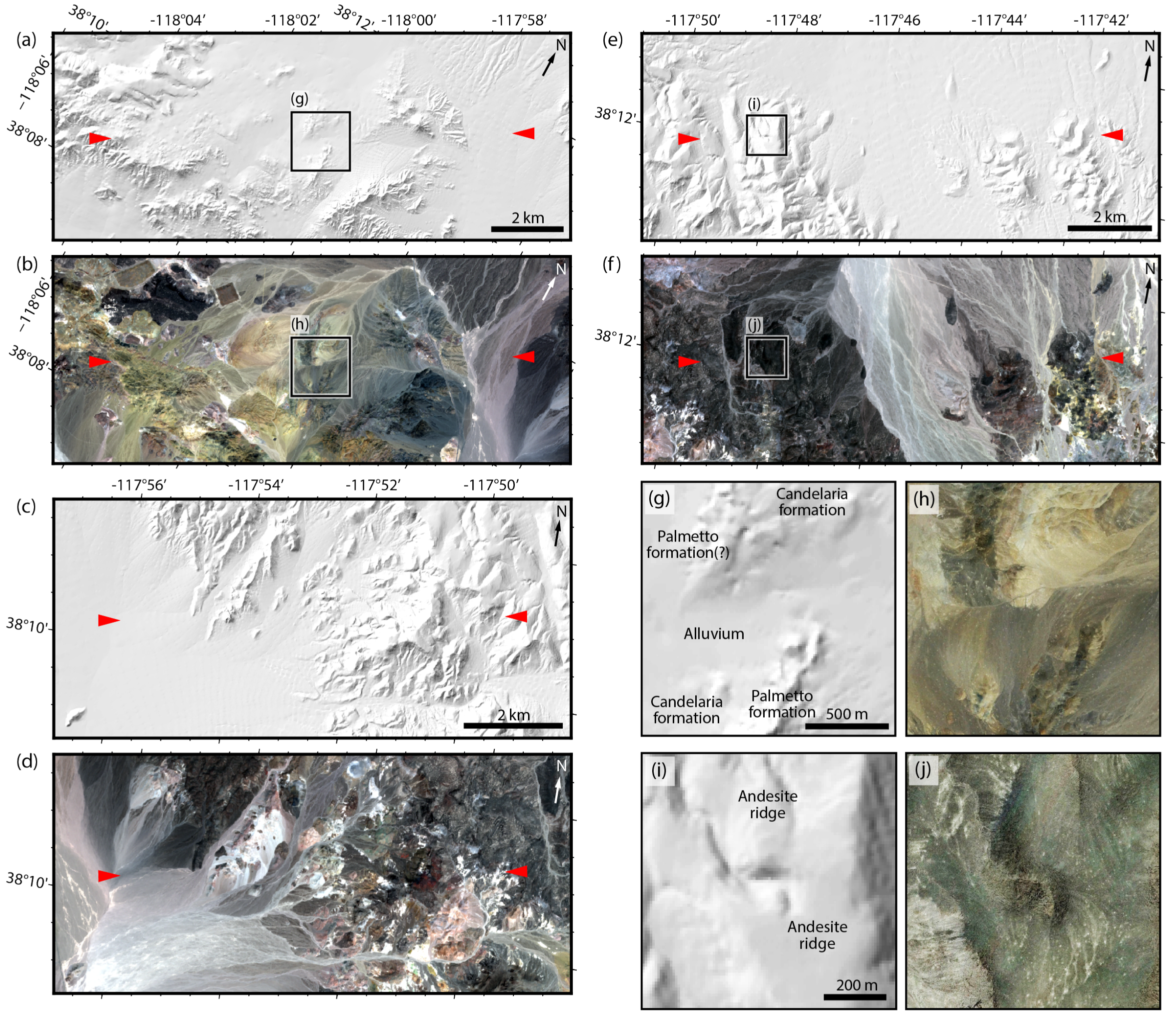

Figure 9. Paired multi-directional hillshaded topography and false color imagery maps along the (a, b) western, (c, d) central, and (e, f) eastern model faults, respectively. The hillshaded topography is the 1/3 arc-second (∼10 m) resolution digital elevation model from the USGS National Map 3D Elevation Program (Fergason et al., 2020). The multi-spectral imagery is from the Sentinel-2B satellite acquired on 3 May 2022, with bands 12-11-2 enhanced using a standard deviation color stretch. Red triangles delineate the model fault endpoints. Boxes denote boundaries of the inset panels g–j showing potential offset ridges used to estimate the cumulative fault offset along the surface projection of the (g, h) western and (i, j) eastern model faults. The satellite photo in the inset figures (h, j) is 2016 Google Earth imagery with our own contrast enhancement.

2002; Dolan & Haravitch, 2014; Zinke et al., 2014; Milliner et al., 2015; C. P. Scott et al., 2018), as postseismic afterslip (Fielding et al., 2009), or as interseismic creep (Fialko et al., 2005; Floyd et al., 2016; Brooks et al., 2017).

We now consider shallow slip deficit in the MCRE in this context, using our own and other published InSAR models (Zheng et al., 2020; Cui et al., 2021; S. Li et al., 2021; Liu et al., 2021) and derived normalized slip profiles calculated using a common 2 km depth increment. Our own model has average surface slip of 0.09 m compared to peak values of 0.59 m at 8–10 km depth (Figure 8a), resulting in an SSD of 86% (Figure 8b). SSDs of the other published models calculated in the same way span between 82–89% except for a lower value of 70% obtained for Cui et al. (2021)'s model. This general agreement implies that the large SSD inferred for the MCRE is robust.

The biggest difference between our normalized slip profiles and those of the other models is our shallower bottom depth, fixed to 12 km on the basis of relocated seismicity. We were therefore interested in the extent to which this could influence the calculated SSD. We test this effect by producing an alternative InSAR-GNSS model in which the fault planes are extended to ∼20 km depth, but with an otherwise identical setup to our preferred model. The 20 km-deep model yields 0.09 m of shallow slip, consistent with our preferred 12 km-deep model, and 0.47 m of peak slip at 6–8 km depth, giving an 82% SSD (Figure 8). The SSDs of our two models are therefore very similar, and extending the bottom depth does not significantly vary the SSD. The main effect of extending the bottom depth is to re-distribute the deeper part of the model slip, resulting in a ∼20% smaller value of peak slip but a ∼20% larger overall moment. This cautions against over-interpreting values of moment obtained from InSAR coseismic slip models, when the bottom depth is not carefully calibrated against seismicity.

The deficit of shallow slip in the MCRE may be compensated through several mechanisms. In the western MCRE rupture zone, fault offsets along the second fracture alignment have maximum offset of ∼20 cm (Dee et al., 2021; Koehler et al., 2021) (Figure 5) and might therefore account for up to around one quarter of the missing shallow deformation. Further east, conjugate surface fractures with up to ∼10 cm of slip could account for an even smaller proportion of the shallow slip deficit. Given the broad deformation field, we expect that there could be additional unmapped subtle off-fault fractures and unmappable features such as folding or volumetric strain which could account for more of the absent shallow deformation. In addition, some amount of the shallow slip deficit may have been compensated by postseismic afterslip, of which only 1–2 days are captured in our interferograms. Hammond et al. (2021) compared coseismic and postseismic surface displacements across the MAGNET GNSS Network within 70 km of the MCRE epicenter over a period of several months. They found that postseismic displacements mimicked coseismic displacement patterns at ∼9–51% of their values, but the long wavelength of this deformation suggests deep rather than shallow afterslip. S. Li et al. (2021) modeled a 6-month InSAR time series and showed that rapid afterslip also occurred at shallow depths of 0–3 km with a peak slip of ∼0.3 m. This likely recovered around another one third of the missing slip, though later afterslip after the study period could potentially raise this contribution further. Any remaining shallow deformation is unlikely to be recovered by aftershocks or future earthquakes since they would need to be centered at unusually shallow depths. Our calibrated relocated aftershocks mostly occur at depths greater than 4 km, exhibit small magnitudes, and are located off the main fault model (Figure 4).

5.5 Does Structural Maturity Control Shallow Slip Deficit?

In the previous two sections, we have demonstrated that the MCRE occurred along a highly immature fault system, and that it involved a pronounced SSD. In this final section, we consider whether these two characteristics are linked by assessing SSDs calculated from InSAR slip models of other continental, strike-slip earthquakes. This extends the work of Dolan and Haravitch (2014), who associated SSD with structural maturity by comparing published subsurface model slip distributions with field offsets of six large (M_w 7.1–7.9) continental strike-slip earthquakes. They found that for earthquake ruptures that occur on structurally mature faults (cumulative displacement ≥85 km), ∼85–95% of slip at depth reaches the surface (equivalent to an SSD of 5–15%), whereas for ruptures on immature faults (cumulative displacement ≤25 km) only ∼50–60% does (SSD of 40–50%). This pattern holds regardless of their geometrical complexity; straight and continuous sections of immature faults still exhibit a pronounced SSD. Dolan and Haravitch (2014) interpret that for ruptures on immature faults, the higher SSD is due to more off-fault deformation at shallow depths, whereas ruptures on mature faults (exhibiting lower SSD) host more localized slip on a principle surface trace.

We investigate this further by comparing our normalized slip profile with those of twenty-seven other continental, strike-slip earthquakes modeled with InSAR (Figure 10a, Table 3). We only consider earthquakes larger than M_w 6.4 since smaller events are less likely to rupture the full seismogenic layer. The geodetic slip profiles are plotted according to the cumulative offset of the host fault (a common proxy for structural maturity) and separately by moment magnitude (Figure 10b,c). We further extract the SSD for each earthquake from the shallowest data point of the slip profile, and compare the value with cumulative offset of the host fault and with moment magnitude (Figures 10d,e). Firstly, our results suggest that SSD does not consistently correlate with cumulative offset (Figure 10d). For instance, the 2020 Elazığ earthquake ruptured the intermediate to mature East Anatolian fault (9–26 km net slip, Duman & Emre, 2013) but exhibits a modeled SSD of 85% (Pousse-Beltran et al., 2020), while the 2019 Ridgecrest earthquakes ruptured very immature faults (<100 m, Gold et al., 2021) with only ∼30 % SSD (Xu et al., 2020). However, the moment magnitude does seem to correlate with SSD, with an R^2 value of 0.55 (Figure 10e). Earthquakes of $M_w > \sim 7$ generally produce smaller SSDs, and $M_w < \sim 7$ events produce larger and more variable SSDs. In this context, the 86% SSD of the MCRE is more a function of its magnitude than its structural immaturity. This pattern can be explained in terms of the earthquake slip budget—moderate sized earthquakes will break to the surface most easily when the hypocenter is shallow but will otherwise leave large SSDs, whereas large earthquakes will rupture more fully to the surface whatever the nucleation depth (Lauer et al., 2020; H. Yang & Yao, 2021; Yao & Yang, 2022).

6 Conclusions

Our InSAR, seismological, and field observations and modeling suggest that the MCRE exhibits complex faulting, with dominant normal-sinistral slip in the west, pure left-lateral motion in the east, and abundant off-fault deformation. Peak geodetic model slip of 1.1 m is buried at 8–10 km depth, and only up to 0.2 m of slip reaches the top 2 km of the crust (yielding a shallow slip deficit of 86%), consistent with at most ∼20 cm of fault offset mapped in the field. The combination of far-field InSAR data and near-field surface fractures and pebble-clearing directions suggests two sub-parallel structures controlling the western MCRE faulting. The mainshock multi-fault geometry and non-double couple focal mechanism, distributed surface fractures, off-fault aftershocks with varying orientations and kinematics, and the limited expression of clear geomorphic features indicative of active faulting are indications that the MCRE ruptured an emergent zone of highly-distributed faulting with little cumulative offset (we estimate it to be ∼600–700 m based on surface geology). However, comparisons with InSAR slip models of twenty-seven other continental, strike-slip earthquakes suggest that the pronounced shallow slip deficit of the MCRE is controlled more by its moderate magnitude than the structural immaturity of its host faults.

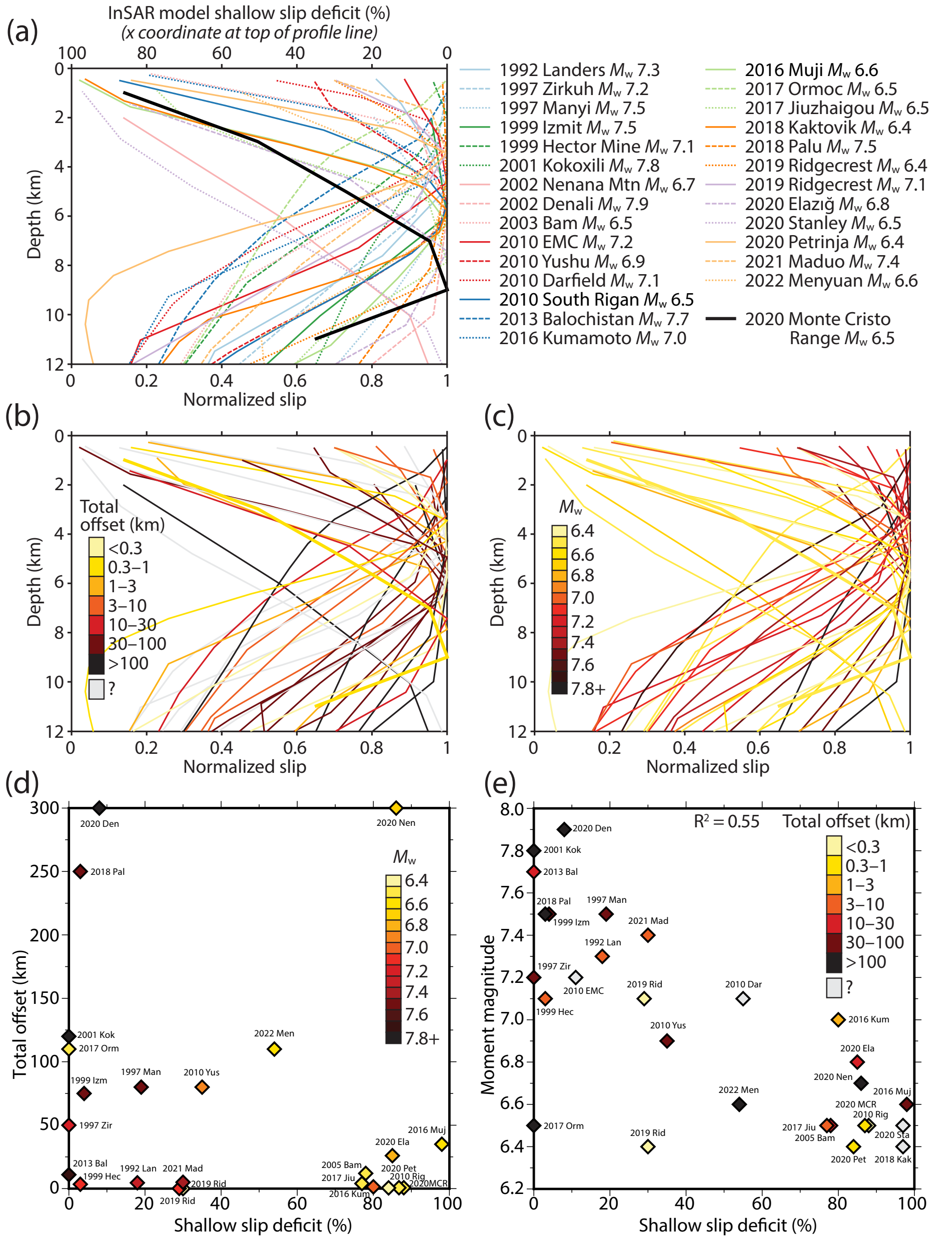

Figure 10. (a) Normalized slip profiles from InSAR-derived coseismic slip models of twenty-eight large (M_w 6.4–7.9), predominantly strike-slip, continental earthquakes. Average slip in each layer of the model is normalized against whichever layer has greatest average slip. The shallow slip deficit annotated along the top of the panel refers to the the shallowest data point of the profile, and is equal to one minus the normalized slip of the surficial row of model sub-fault patches expressed as a percentage (e.g., Fialko et al., 2005). InSAR model references are given in Table 3. (b) Normalized slip profiles colored by the total geological offset accumulated by the host fault (see Table 3 for offset values and references). (c) Normalized slip profiles colored by moment magnitude. (d, e) Scatter plots between shallow slip deficit in percentage versus (d) total offset in km (colored by moment magnitude), and (e) moment magnitude (colored by total offset). Earthquakes with unknown cumulative offsets on the host fault are excluded from panel (d). Data points are labeled with the event year and the first three letters of the event name, unless noted in Table 3.

Table 3. List of earthquakes, InSAR model shallow slip deficits, and cumulative, geological offsets for the earthquakes profiled in Figure 10 (EMC = El Mayor-Cucapah; MCR = Monte Cristo Range). For each InSAR model, the shallow slip deficit is equal to one minus the normalized slip of the surficial row of model sub-fault patches (the shallowest data point of the profile in Figure 10), expressed as a percentage (e.g., Fialko et al., 2005). We recognize that many of these earthquakes have multiple published InSAR models, only one of which is presented here. Slip models that also incorporate near-field displacement fields from optical image correlation or differential lidar are asterisked.

Earthquake	M_w	InSAR model shallow slip deficit		Total geological offset	
		Value	Source	Value	Source
1992 Landers	7.3	18%	Xu et al. (2016)*	3.1–4.6 km	Jachens (2002)
1997 Manyi	7.5	19%	Funning et al. (2007)	∼20–80 km	Zhikun Ren, pers. comm.
1997 Zirkuh	7.2	0%	Marchandon et al. (2018)*	∼10–50 km	Richard Walker, pers. comm.
1999 Izmit	7.5	4%	Çakir et al. (2003)	∼4–75 km	Şengör et al. (2005)
1999 Hector Mine	7.1	3%	Xu et al. (2016)*	3.4 km	Jachens (2002)
2001 Kokoxili	7.8	0%	Lasserre et al. (2005)	100 ±20 km	Fu and Awata (2007)
2002 Nenana Mtn[a]	6.7	86%	Wright et al. (2003)	∼300 km	Eisbacher (1976)
2002 Denali	7.9	8%	Wright et al. (2004)	∼300 km	Eisbacher (1976)
2003 Bam	6.5	78%	Fialko et al. (2005)	$\ll$12 km	Jackson et al. (2006)
2010 EMC	7.2	11%	Xu et al. (2016)*	Mixed/unknown	Fletcher et al. (2014)
2010 Yushu	6.9	35%	Z. Li et al. (2011)	39–80 km	S. Wang et al. (2008)
2010 Rigan	6.5	87%	Walker et al. (2013)	Probably small	Walker et al. (2013)
2010 Darfield	7.1	55%	Elliott et al. (2012)	Unknown	Jongens et al. (2012)
2013 Balochistan	7.7	0%	Lauer et al. (2020)*	∼11 km	Zinke et al. (2014)
2016 Kumamoto	7.0	80%	C. Scott et al. (2019)*	800–1400 m	C. P. Scott et al. (2018)
2016 Muji	6.6	98%	W. Feng et al. (2017)	∼30–35 km	Li Tao, pers. comm.
2017 Ormoc	6.5	0%	Y. H. Yang et al. (2018)	∼110 km	Cole et al. (1989)
2017 Jiuzhaigou	6.5	77%	Y. Li et al. (2020)	1–4 km	C. Li et al. (2019)
2018 Kaktovik	6.4	97%	Gaudreau et al. (2019)	Unknown	–
2018 Palu	7.5	3%	Socquet et al. (2019)*	150–250 km	Silver et al. (1983)
2019 Ridgecrest	6.4	30%	Xu et al. (2020)*	<20 m	Gold et al. (2021)
2019 Ridgecrest	7.1	29%	Xu et al. (2020)*	<100 m	Gold et al. (2021)
2020 Elazığ	6.8	85%	Pousse-Beltran et al. (2020)	9–26 km	Duman and Emre (2013)
2020 Stanley[a]	6.5	97%	J. Yang et al. (2021)	Unknown	–
2020 MCR	6.5	88%	This study	∼600–700 m	This study
2020 Petrinja	6.4	84%	Xiong et al. (2022)	∼560 m	Baize et al. (2022)
2021 Maduo	7.4	30%	Jin and Fialko (2021)	∼2.5–5 km	Li Tao/Jinrui Liu, pers. comm.
2022 Menyuan	6.6	54%	H. Yang et al. (2022)	95 ±15 km	Gaudemer et al. (1995)

[a] InSAR model slip in the 2002 Nenana Mountain and the 2020 Stanley earthquakes peaks at 14 km and 12.5 km depth, respectively (Wright et al., 2003; J. Yang et al., 2021).

Acknowledgments

We are very grateful to Harley Benz for kindly helping us with the regional moment tensor solutions and for his support and encouragement of our work. This study is funded through grants from the Natural Science and Engineering Research Council of Canada (NSERC), the Canada Foundation for Innovation (CFI), and the BC Knowledge Development Fund (BCKDF), as well as a University of Victoria Graduate Award, a James A. & Laurette Agnew Memorial Award, and an Anand-UVic Fund Graduate Scholarship to I.S., a Tier 2 Canada Research Chair to E.N., and a Leverhulme Trust project 'EROICA' to I.P. All data used in this study are freely available through the following platforms. SAR and multispectral images from Sentinel-1 and -2 satellites were accessed

from the Alaska Satellite Facility (https://search.asf.alaska.edu) and the Copernicus Open Access Hub (https://scihub.copernicus.eu). We used digital elevation models obtained from OpenTopography (https://opentopography.org), GMTSAR (https://topex.ucsd.edu/gmtsar/demgen), and the USGS 3DEP (https://apps.nationalmap.gov/downloader). Earthquake arrival times were collected from the ISC Bulletin (https://doi.org/10.31905/D808B830) and the ANSS ComCat system (https://doi.org/10.5066/P95R8K8G). Regional waveform data were obtained from NEIC and the Nevada Seismological Laboratory, UNR. The GNSS coseismic offsets (19 June 2020 data set) were obtained from NGL (http://geodesy.unr.edu/news_items/20200619/ Jun-2020.txt). Reproducible InSAR and seismological results from this study are tabulated in Table 2 and Supplementary data files C1–C3. Figures were plotted using the Generic Mapping Tools version 6 (Wessel et al., 2019).

References

Aben, F. M., Doan, M. L., Mitchell, T. M., Toussaint, R., Reuschlé, T., Fondriest, M., ... Renard, F. (2016). Dynamic fracturing by successive coseismic loadings leads to pulverization in active fault zones. *Journal of Geophysical Research: Solid Earth*, *121*(4), 2338–2360. doi: 10.1002/2015JB012542

Aderhold, K., & Abercrombie, R. E. (2015). Seismic Rupture on an Oceanic-Continental Plate Boundary: Strike-Slip Earthquakes along the Queen Charlotte-Fairweather Fault. *Bulletin of the Seismological Society of America*, *105*(2B), 1129–1142. doi: 10.1785/0120140227

Amoruso, A., Crescentini, L., & Fidani, C. (2004). Effects of crustal layering on source parameter inversion from coseismic geodetic data. *Geophysical Journal International*, *159*(1), 353–364. doi: 10.1111/j.1365-246X.2004.02389.x

Baize, S., Amoroso, S., Belić, N., Benedetti, L., Boncio, P., Budić, M., ... Ricci, T. (2022). Environmental effects and seismogenic source characterization of the December 2020 earthquake sequence near Petrinja, Croatia. *Geophysical Journal International*, *230*(2), 1394–1418. doi: 10.1093/gji/ggac123

Barbot, S., Fialko, Y., & Sandwell, D. (2008). Effect of a compliant fault zone on the inferred earthquake slip distribution. *Journal of Geophysical Research: Solid Earth*, *113*(B6), B06404. doi: 10.1029/2007JB005256

Bennett, R. A., Wernicke, B. P., Niemi, N. A., Friedrich, A. M., & Davis, J. L. (2003). Contemporary strain rates in the northern Basin and Range province from GPS data. *Tectonics*, *22*(2), 1008. doi: 10.1029/2001TC001355

Benz, H. M. (2021). Global catalog of calibrated earthquake locations. *US Geological Survey Data Release*. doi: 10.5066/P95R8K8G

Berberian, M., Jackson, J. A., Fielding, E., Parsons, B. E., Priestley, K., Qorashi, M., ... Baker, C. (2001). The 1998 March 14 Fandoqa earthquake (M_w 6.6) in Kerman province, southeast Iran: re-rupture of the 1981 Sirch earthquake fault, triggering of slip on adjacent thrusts and the active tectonics of the Gowk fault zone. *Geophysical Journal International*, *146*(2), 371–398. doi: 10.1046/j.0956-540X.2001.01459.x

Bergman, E. A., & Solomon, S. C. (1990). Earthquake swarms on the Mid-Atlantic Ridge: Products of magmatism or extensional tectonics? *Journal of Geophysical Research: Solid Earth*, *95*(B4), 4943–4965. doi: 10.1029/JB095iB04p04943

Berryman, K. R., Cochran, U. A., Clark, K. J., Biasi, G. P., Langridge, R. M., & Villamor, P. (2012). Major Earthquakes Occur Regularly on an Isolated Plate Boundary Fault. *Science*, *336*(6089), 1690. doi: 10.1126/science.1218959

Blewitt, G., Hammond, W. C., & Kreemer, C. (2018). Harnessing the GPS data explosion for interdisciplinary science. *Eos*, *99*(10.1029), 485. doi: 10.1029/2018EO104623

Bormann, J. M., Hammond, W. C., Kreemer, C., & Blewitt, G. (2016). Accommodation of missing shear strain in the Central Walker Lane, western North

America: Constraints from dense GPS measurements. *Earth and Planetary Science Letters*, *440*, 169–177. doi: 10.1016/j.epsl.2016.01.015

Bormann, J. M., Morton, E. A., Smith, K. D., Kent, G. M., Honjas, W. S., Plank, G. L., & Williams, M. C. (2021). Nevada Seismological Laboratory Rapid Seismic Monitoring Deployment and Data Availability for the 2020 M_{ww} 6.5 Monte Cristo Range, Nevada, Earthquake Sequence. *Seismological Research Letters*, *92*(2A), 810–822. doi: 10.1785/0220200344

Bro, R., & De Jong, S. (1997). A fast non-negativity-constrained least squares algorithm. *Journal of Chemometrics*, *11*(5), 393–401. doi: 10.1002/(SICI)1099-128X(199709/10)11:5\textless{}393::AID-CEM483\textgreater{}3.0.CO;2-L

Brodsky, E. E., Gilchrist, J. J., Sagy, A., & Collettini, C. (2011). Faults smooth gradually as a function of slip. *Earth and Planetary Science Letters*, *302*(1–2), 185-193. doi: 10.1016/j.epsl.2010.12.010

Brooks, B. A., Minson, S. E., Glennie, C. L., Nevitt, J. M., Dawson, T., Rubin, R., … Zaccone, D. (2017). Buried shallow fault slip from the South Napa earthquake revealed by near-field geodesy. *Science Advances*, *3*(7), e1700525. doi: 10.1126/sciadv.1700525

Callaghan, E., & Gianella, V. P. (1935). The earthquake of January 30, 1934, at Excelsior Mountains, Nevada. *Bulletin of the Seismological Society of America*, *25*(2), 161–168. doi: 10.1785/BSSA0250020161

Çakir, Z., de Chabalier, J.-B., Armijo, R., Meyer, B., Barka, A., & Peltzer, G. (2003). Coseismic and early post-seismic slip associated with the 1999 Izmit earthquake (Turkey), from SAR interferometry and tectonic field observations. *Geophysical Journal International*, *155*(1), 93–110. doi: 10.1046/j.1365-246X.2003.02001.x

Childs, C., Manzocchi, T., Walsh, J. J., Bonson, C. G., Nicol, A., & Schöpfer, M. P. J. (2009). A geometric model of fault zone and fault rock thickness variations. *Journal of Structural Geology*, *31*(2), 117–127. doi: 10.1016/j.jsg.2008.08.009

Childs, C., Watterson, J., & Walsh, J. J. (1995, May). Fault overlap zones within developing normal fault systems. *Journal of the Geological Society*, *152*(3), 535–549. doi: 10.1144/gsjgs.152.3.0535

Chounet, A., Vallée, M., Causse, M., & Courboulex, F. (2018). Global catalog of earthquake rupture velocities shows anticorrelation between stress drop and rupture velocity. *Tectonophysics*, *733*, 148-158. doi: 10.1016/j.tecto.2017.11.005

Choy, G. L., & Kirby, S. H. (2004). Apparent stress, fault maturity and seismic hazard for normal-fault earthquakes at subduction zones. *Geophysical Journal International*, *159*(3), 991–1012. doi: 10.1111/j.1365-246X.2004.02449.x

Cole, J., McCabe, R., Moriarty, T., Malicse, J. A., Delfin, F. G., Tebar, H., & Ferrer, H. P. (1989). A preliminary Neogene paleomagnetic data set from Leyte and its relation to motion on the Philippine fault. *Tectonophysics*, *168*(1), 205–220. doi: 10.1016/0040-1951(89)90376-4

Cui, Y., Ma, Z., Aoki, Y., Liu, J., Yue, D., Hu, J., … Li, Z. (2021). Refining slip distribution in moderate earthquakes using Sentinel-1 burst overlap interferometry: a case study over 2020 May 15 M_w 6.5 Monte Cristo Range Earthquake. *Geophysical Journal International*, *229*, 472–486. doi: 10.1093/gji/ggab492

Dee, S., Koehler, R. D., Elliott, A. J., Hatem, A. E., Pickering, A., Pierce, I., … Zachariasen, J. (2021). *Surface rupture map of the 2020 M 6.5 Monte Cristo range earthquake, Esmeralda and Mineral counties, Nevada* (Tech. Rep. No. 190). Reno, Nevada: University of Nevada, Reno.

DeLano, K., Lee, J., Roper, R., & Calvert, A. (2019). Dextral, normal, and sinistral faulting across the eastern California shear zone-Mina deflection transition, California-Nevada, USA. *Geosphere*, *15*(4), 1206–1239. doi: 10.1130/GES01636.1

Dohrenwend, J. C. (1982). *Surficial geologic map of the Walker Lake 1 degree × 2 degrees quadrangle, Nevada-California* (Tech. Rep. No. Miscellaneous Field Studies Map MF-1382-C). Denver, Colorado: U.S. Geological Survey.

Dokka, R. K., & Travis, C. J. (1990). Role of the Eastern California Shear Zone in accommodating Pacific-North American Plate motion. *Geophysical Research Letters*, *17*(9), 1323–1326. doi: 10.1029/GL017i009p01323

Dolan, J. F., & Haravitch, B. D. (2014). How well do surface slip measurements track slip at depth in large strike-slip earthquakes? The importance of fault structural maturity in controlling on-fault slip versus off-fault surface deformation. *Earth and Planetary Science Letters*, *388*, 38–47. doi: 10.1016/j.epsl.2013.11.043

Duman, T. Y., & Emre, O. (2013). The East Anatolian Fault: geometry, segmentation and jog characteristics. *Geological Society of London Special Publications*, *372*(1), 495-529. doi: 10.1144/SP372.14

Eisbacher, G. H. (1976). Sedimentology of the Dezadeash flysch and its implications for strike-slip faulting along the Denali Fault, Yukon Territory and Alaska. *Canadian Journal of Earth Sciences*, *13*(11), 1495-1513. doi: 10.1139/e76-157

Elliott, J. R., Bergman, E. A., Copley, A. C., Ghods, A. R., Nissen, E. K., Oveisi, B., ... Yamini-Fard, F. (2015). The 2013 M_w 6.2 Khaki-Shonbe (Iran) Earthquake: Insights into seismic and aseismic shortening of the Zagros sedimentary cover. *Earth and Space Science*, *2*(11), 435–471. doi: 10.1002/2015EA000098

Elliott, J. R., Nissen, E. K., England, P. C., Jackson, J. A., Lamb, S., Li, Z., ... Parsons, B. (2012). Slip in the 2010-2011 Canterbury earthquakes, New Zealand. *Journal of Geophysical Research: Solid Earth*, *117*(B3), B03401. doi: 10.1029/2011JB008868

Elliott, J. R., Parsons, B., Jackson, J. A., Shan, X., Sloan, R. A., & Walker, R. T. (2011). Depth segmentation of the seismogenic continental crust: The 2008 and 2009 Qaidam earthquakes. *Geophysical Research Letters*, *38*(6), L06305. doi: 10.1029/2011GL046897

Farr, T. G., & Kobrick, M. (2000). Shuttle radar topography mission produces a wealth of data. *EOS Transactions*, *81*(48), 583–585. doi: 10.1029/EO081i048p00583

Faulkner, D. R., Mitchell, T. M., Jensen, E., & Cembrano, J. (2011). Scaling of fault damage zones with displacement and the implications for fault growth processes. *Journal of Geophysical Research: Solid Earth*, *116*(B5), B05403. doi: 10.1029/2010JB007788

Feng, L., Newman, A. V., Farmer, G. T., Psimoulis, P., & Stiros, S. C. (2010). Energetic rupture, coseismic and post-seismic response of the 2008 M_W 6.4 Achaia-Elia Earthquake in northwestern Peloponnese, Greece: an indicator of an immature transform fault zone. *Geophysical Journal International*, *183*(1), 103–110. doi: 10.1111/j.1365-246X.2010.04747.x

Feng, W., Tian, Y., Zhang, Y., Samsonov, S., Almeida, R., & Liu, P. (2017). A slip gap of the 2016 M_w 6.6 Muji, Xinjiang, China, earthquake inferred from Sentinel-1 TOPS interferometry. *Seismological Research Letters*, *88*(4), 1054–1064.

Fergason, R. L., Hare, T. M., Mayer, D. P., Galuszka, D. M., Redding, B. L., Smith, E. D., ... Otero, R. E. (2020). Mars 2020 terrain relative navigation flight product generation: Digital terrain model and orthorectified image mosaic. In *Lunar and planetary science conference.*

Ferguson, H. G., Muller, S. W., & Cathcart, S. H. (1953). *Geology of the Coaldale quadrangle, Nevada* (Tech. Rep. No. Geologic Quadrangle Map GQ-23). Denver, Colorado: U.S. Geological Survey.

Ferguson, H. G., Muller, S. W., & Cathcart, S. H. (1954). *Geology of the Mina quadrangle, Nevada* (Tech. Rep. No. Geologic Quadrangle Map GQ-45). Den-

ver, Colorado: U.S. Geological Survey.
Fialko, Y., Sandwell, D., Simons, M., & Rosen, P. (2005). Three-dimensional deformation caused by the Bam, Iran, earthquake and the origin of shallow slip deficit. *Nature*, *435*(7040), 295–299. doi: 10.1038/nature03425
Fielding, E. J., Lundgren, P. R., Bürgmann, R., & Funning, G. J. (2009). Shallow fault-zone dilatancy recovery after the 2003 Bam earthquake in Iran. *Nature*, *458*(7234), 64–68. doi: 10.1038/nature07817
Finzi, Y., Hearn, E. H., Ben-Zion, Y., & Lyakhovsky, V. (2009). Structural Properties and Deformation Patterns of Evolving Strike-slip Faults: Numerical Simulations Incorporating Damage Rheology. *Pure and Applied Geophysics*, *166*(10–11), 1537–1573. doi: 10.1007/s00024-009-0522-1
Fletcher, J. M., Teran, O. J., Rockwell, T. K., Oskin, M. E., Hudnut, K. W., Mueller, K. J., … González-García, J. (2014). Assembly of a large earthquake from a complex fault system: Surface rupture kinematics of the 4 April 2010 El Mayor-Cucapah (Mexico) M_w 7.2 earthquake. *Geosphere*, *10*(4), 797–827. doi: 10.1130/GES00933.1
Floyd, M. A., Walters, R. J., Elliott, J. R., Funning, G. J., Svarc, J. L., Murray, J. R., … Wright, T. J. (2016). Spatial variations in fault friction related to lithology from rupture and afterslip of the 2014 South Napa, California, earthquake. *Geophysical Research Letters*, *43*(13), 6808–6816. doi: 10.1002/2016GL069428
Frost, E., Dolan, J., Sammis, C., Hacker, B., Cole, J., & Ratschbacher, L. (2009). Progressive strain localization in a major strike-slip fault exhumed from midseismogenic depths: Structural observations from the Salzach-Ennstal-Mariazell-Puchberg fault system, Austria. *Journal of Geophysical Research: Solid Earth*, *114*(B4), B04406. doi: 10.1029/2008JB005763
Fu, B., & Awata, Y. (2007). Displacement and timing of left-lateral faulting in the Kunlun Fault Zone, northern Tibet, inferred from geologic and geomorphic features. *Journal of Asian Earth Sciences*, *29*(2–3), 253–265. doi: 10.1016/j.jseaes.2006.03.004
Funning, G. J., Parsons, B., & Wright, T. J. (2007). Fault slip in the 1997 Manyi, Tibet earthquake from linear elastic modelling of InSAR displacements. *Geophysical Journal International*, *169*(3), 988–1008.
Funning, G. J., Parsons, B., Wright, T. J., Jackson, J. A., & Fielding, E. J. (2005). Surface displacements and source parameters of the 2003 Bam (Iran) earthquake from Envisat advanced synthetic aperture radar imagery. *Journal of Geophysical Research: Solid Earth*, *110*(B9), B09406. doi: 10.1029/2004JB003338
Gaudemer, Y., Tapponnier, P., Meyer, B., Peltzer, G., Shunmin, G., Zhitai, C., … Cifuentes, I. (1995, March). Partitioning of crustal slip between linked, active faults in the eastern Qilian Shan, and evidence for a major seismic gap, the 'Tianzhu gap', on the western Haiyuan Fault, Gansu (China). *Geophysical Journal International*, *120*(3), 599–645. doi: 10.1111/j.1365-246X.1995.tb01842.x
Gaudreau, É., Nissen, E. K., Bergman, E. A., Benz, H. M., Tan, F., & Karasözen, E. (2019). The August 2018 Kaktovik Earthquakes: Active Tectonics in Northeastern Alaska Revealed With InSAR and Seismology. *Geophysical Research Letters*, *46*(24), 14,412-14,420. doi: 10.1029/2019GL085651
Gold, R. D., DuRoss, C. B., & Barnhart, W. D. (2021). Coseismic Surface Displacement in the 2019 Ridgecrest Earthquakes: Comparison of Field Measurements and Optical Image Correlation Results. *Geochemistry, Geophysics, Geosystems*, *22*(3), e09326.
Goldstein, R. M., & Werner, C. L. (1998). Radar interferogram filtering for geophysical applications. *Geophysical Research Letters*, *25*(21), 4035–4038. doi: 10.1029/1998GL900033

Gomberg, J. (1996, January). Stress/strain changes and triggered seismicity following the M_w 7.3 Landers, California earthquake. *Journal of Geophysical Research: Solid Earth*, *101*(B1), 751–764. doi: 10.1029/95JB03251

Grondin, D. P., Petronis, M., Lindline, J., & Romero, B. P. (2016). Vertical axis clockwise rotation of fault blocks in the eastern Mono Basin, California and Nevada. In *Geological society of america abstracts with programs* (Vol. 48). doi: 10.1130/abs/2016AM-286303

Hamling, I. J., Hreinsdóttir, S., Clark, K., Elliott, J., Liang, C., Fielding, E., ... Stirling, M. (2017). Complex multifault rupture during the 2016 M_w 7.8 Kaikōura earthquake, New Zealand. *Science*, *356*(6334). doi: 10.1126/science.aam7194

Hammond, W. C., Blewitt, G., Kreemer, C., Koehler, R. D., & Dee, S. (2021). Geodetic Observation of Seismic Cycles before, during, and after the 2020 Monte Cristo Range, Nevada Earthquake. *Seismological Research Letters*, *92*(2A), 647–662. doi: 10.1785/0220200338

Hatem, A. E., Cooke, M. L., & Toeneboehn, K. (2017). Strain localization and evolving kinematic efficiency of initiating strike-slip faults within wet kaolin experiments. *Journal of Structural Geology*, *101*, 96–108. doi: 10.1016/j.jsg.2017.06.011

Hearn, E. H., & Bürgmann, R. (2005). The Effect of Elastic Layering on Inversions of GPS Data for Coseismic Slip and Resulting Stress Changes: Strike-Slip Earthquakes. *Bulletin of the Seismological Society of America*, *95*(5), 1637–1653. doi: 10.1785/0120040158

Hecker, S., Dawson, T. E., & Schwartz, D. P. (2010). Normal-Faulting Slip Maxima and Stress-Drop Variability: A Geological Perspective. *Bulletin of the Seismological Society of America*, *100*(6), 3130–3147. doi: 10.1785/0120090356

Herrmann, R. B., Benz, H., & Ammon, C. J. (2011). Monitoring the Earthquake Source Process in North America. *Bulletin of the Seismological Society of America*, *101*(6), 2609–2625.

Hicks, S. P., & Rietbrock, A. (2015, December). Seismic slip on an upper-plate normal fault during a large subduction megathrust rupture. *Nature Geoscience*, *8*(12), 955–960. doi: 10.1038/ngeo2585

Hodgkinson, K. M., Stein, R. S., & King, G. C. P. (1996). The 1954 Rainbow Mountain-Fairview Peak-Dixie Valley earthquakes: A triggered normal faulting sequence. *Journal of Geophysical Research: Solid Earth*, *101*(B11), 25459–25471. doi: 10.1029/96JB01302

Huang, M. H., Fielding, E. J., Dickinson, H., Sun, J., Gonzalez-Ortega, J. A., Freed, A. M., & Bürgmann, R. (2017). Fault geometry inversion and slip distribution of the 2010 M_w 7.2 El Mayor-Cucapah earthquake from geodetic data. *Journal of Geophysical Research: Solid Earth*, *122*(1), 607–621. doi: 10.1002/2016JB012858

Huang, M.-H., Tung, H., Fielding, E. J., Huang, H.-H., Liang, C., Huang, C., & Hu, J.-C. (2016, July). Multiple fault slip triggered above the 2016 M_w 6.4 MeiNong earthquake in Taiwan. *Geophysical Research Letters*, *43*(14), 7459–7467. doi: 10.1002/2016GL069351

Hull, J. (1988). Thickness-displacement relationships for deformation zones. *Journal of Structural Geology*, *10*(4), 431–435. doi: 10.1016/0191-8141(88)90020-X

Hutchison, A. A., Böse, M., & Manighetti, I. (2020). Improving Early Estimates of Large Earthquake's Final Fault Lengths and Magnitudes Leveraging Source Fault Structural Maturity Information. *Geophysical Research Letters*, *47*(14), e87539. doi: 10.1029/2020GL087539

Jachens, R. C. (2002). Relationship of the 1999 Hector Mine and 1992 Landers Fault Ruptures to Offsets on Neogene Faults and Distribution of Late Cenozoic Basins in the Eastern California Shear Zone. *Bulletin of the Seismological Society of America*, *92*(4), 1592–1605. doi: 10.1785/0120000915

Jackson, J., Bouchon, M., Fielding, E., Funning, G., Ghorashi, M., Hatzfeld, D., ... Wright, T. (2006). Seismotectonic, rupture process, and earthquake-hazard aspects of the 2003 December 26 Bam, Iran, earthquake. *Geophysical Journal International*, *166*(3), 1270–1292. doi: 10.1111/j.1365-246X.2006.03056.x

Jin, Z., & Fialko, Y. (2021). Coseismic and Early Postseismic Deformation Due to the 2021 M7.4 Maduo (China) Earthquake. *Geophysical Research Letters*, *48*(21), e95213.

Johanson, I. A., Fielding, E. J., Rolandone, F., & Bürgmann, R. (2006). Coseismic and postseismic slip of the 2004 Parkfield earthquake from space-geodetic data. *Bulletin of the Seismological Society of America*, *96*(4B), 269–282.

Jongens, R., Barrell, D. J. A., Campbell, J. K., & Pettinga, J. R. (2012). Faulting and folding beneath the Canterbury Plains identified prior to the 2010 emergence of the Greendale Fault. *New Zealand Journal of Geology and Geophysics*, *55*(3), 169–176.

Jónsson, S., Zebker, H., Segall, P., & Amelung, F. (2002). Fault slip distribution of the 1999 M_w 7.1 Hector Mine, California, earthquake, estimated from satellite radar and GPS measurements. *Bulletin of the Seismological Society of America*, *92*(4), 1377–1389.

Kane, D. L., Shearer, P. M., Goertz-Allmann, B. P., & Vernon, F. L. (2013). Rupture directivity of small earthquakes at Parkfield. *Journal of Geophysical Research: Solid Earth*, *118*(1), 212–221. doi: 10.1029/2012JB009675

Kaneko, Y., & Fialko, Y. (2011). Shallow slip deficit due to large strike-slip earthquakes in dynamic rupture simulations with elasto-plastic off-fault response. *Geophysical Journal International*, *186*(3), 1389–1403. doi: 10.1111/j.1365-246X.2011.05117.x

Kaneko, Y., Lapusta, N., & Ampuero, J. P. (2008). Spectral element modeling of spontaneous earthquake rupture on rate and state faults: Effect of velocity-strengthening friction at shallow depths. *Journal of Geophysical Research: Solid Earth*, *113*(B9), B09317. doi: 10.1029/2007JB005553

Karasözen, E., Nissen, E., Bergman, E. A., & Ghods, A. (2019). Seismotectonics of the Zagros (Iran) From Orogen-Wide, Calibrated Earthquake Relocations. *Journal of Geophysical Research: Solid Earth*, *124*(8), 9109–9129. doi: 10.1029/2019JB017336

Kennett, B. L. N., Engdahl, E. R., & Buland, R. (1995). Constraints on seismic velocities in the Earth from traveltimes. *Geophysical Journal International*, *122*(1), 108–124. doi: 10.1111/j.1365-246X.1995.tb03540.x

Klinger, Y. (2010, jul). Relation between continental strike-slip earthquake segmentation and thickness of the crust. *Journal of Geophysical Research: Solid Earth*, *115*(7), B07306. doi: 10.1029/2009JB006550

Koehler, R. D., Dee, S., Elliott, A., Hatem, A., Pickering, A., Pierce, I., & Seitz, G. (2021). Field Response and Surface-Rupture Characteristics of the 2020 M 6.5 Monte Cristo Range Earthquake, Central Walker Lane, Nevada. *Seismological Research Letters*, *92*(2A), 823–839. doi: 10.1785/0220200371

Lasserre, C., Peltzer, G., Crampé, F., Klinger, Y., van der Woerd, J., & Tapponnier, P. (2005). Coseismic deformation of the 2001 $M_w = 7.8$ Kokoxili earthquake in Tibet, measured by synthetic aperture radar interferometry. *Journal of Geophysical Research: Solid Earth*, *110*(B12), B12408. doi: 10.1029/2004JB003500

Lauer, B., Grandin, R., & Klinger, Y. (2020). Fault Geometry and Slip Distribution of the 2013 Mw 7.7 Balochistan Earthquake From Inversions of SAR and Optical Data. *Journal of Geophysical Research: Solid Earth*, *125*(7), e18380. doi: 10.1029/2019JB018380

Lee, J., Garwood, J., Stockli, D. F., & Gosse, J. (2009). Quaternary faulting in Queen Valley, California-Nevada: Implications for kinematics of fault-slip transfer in the eastern California shear zone-Walker Lane belt. *Geological*

Society of America Bulletin, *121*(3–4), 599–614. doi: 10.1130/B26352.1

Lee, J., Stockli, D., Schroeder, J., Tincher, C., Bradley, D., Owen, L., ... Garwood, J. (2006). *Fault Slip Transfer in the Eastern California Shear Zone-Walker Lane Belt.* Geological Society of America Penrose Conference Field Trip Guide (Kinematics and Geodynamics of Intraplate Dextral Shear in Eastern California and Western Nevada, Mammoth Lakes, California, 21–26 April 2005). doi: 10.1130/2006.FSTITE.PFG

Li, C., Wang, X., He, C., Wu, X., Kong, Z., & Li, X. (2019). China National Digital Geological Map (Public Version at 1:200 000 Scale) Spatial Database. *Geology in China*, *46*(S1), 1–10. doi: 10.23650/data.A.2019.NGA120157.K1.1.1.V1

Li, S., Tao, T., Chen, Y., He, P., Gao, F., Qu, X., & Zhu, Y. (2021). Geodetic Observation and Modeling of the Coseismic and Postseismic Deformations Associated With the 2020 Mw 6.5 Monte Cristo Earthquake. *Earth and Space Science*, *8*(6), e01696. doi: 10.1029/2021EA001696

Li, Y., Bürgmann, R., & Zhao, B. (2020). Evidence of Fault Immaturity from Shallow Slip Deficit and Lack of Postseismic Deformation of the 2017 M_w 6.5 Jiuzhaigou Earthquake. *Bulletin of the Seismological Society of America*, *110*(1), 154–165. doi: 10.1785/0120190162

Li, Z., Elliott, J. R., Feng, W., Jackson, J. A., Parsons, B. E., & Walters, R. J. (2011). The 2010 M_W 6.8 Yushu (Qinghai, China) earthquake: Constraints provided by InSAR and body wave seismology. *Journal of Geophysical Research: Solid Earth*, *116*(B10), B10302. doi: 10.1029/2011JB008358

Lindsey, E. O., Sahakian, V. J., Fialko, Y., Bock, Y., Barbot, S., & Rockwell, T. K. (2014). Interseismic Strain Localization in the San Jacinto Fault Zone. *Pure and Applied Geophysics*, *171*(11), 2937–2954. doi: 10.1007/s00024-013-0753-z

Liu, C., Lay, T., Pollitz, F. F., Xu, J., & Xiong, X. (2021). Seismic and Geodetic Analysis of Rupture Characteristics of the 2020 M_w 6.5 Monte Cristo Range, Nevada, Earthquake. *Bulletin of the Seismological Society of America*, *111*(6), 3226–3236. doi: 10.1785/0120200327

Locke, A., Billingsley, P., & Mayo, E. B. (1940). Sierra Nevada tectonic pattern. *Geological Society of America Bulletin*, *51*(4), 513–539. doi: 10.1130/GSAB-51-513

Mackenzie, D., Elliott, J. R., Altunel, E., Walker, R. T., Kurban, Y. C., Schwenninger, J. L., & Parsons, B. (2016). Seismotectonics and rupture process of the M_W 7.1 2011 Van reverse-faulting earthquake, eastern Turkey, and implications for hazard in regions of distributed shortening. *Geophysical Journal International*, *206*(1), 501–524. doi: 10.1093/gji/ggw158

Manighetti, I., Campillo, M., Bouley, S., & Cotton, F. (2007). Earthquake scaling, fault segmentation, and structural maturity. *Earth and Planetary Science Letters*, *253*(3–4), 429–438. doi: 10.1016/j.epsl.2006.11.004

Manighetti, I., Mercier, A., & De Barros, L. (2021). Fault Trace Corrugation and Segmentation as a Measure of Fault Structural Maturity. *Geophysical Research Letters*, *48*(20), e95372. doi: 10.1029/2021GL095372

Marchandon, M., Hollingsworth, J., & Radiguet, M. (2021, January). Origin of the shallow slip deficit on a strike slip fault: Influence of elastic structure, topography, data coverage, and noise. *Earth and Planetary Science Letters*, *554*, 116696. doi: 10.1016/j.epsl.2020.116696

Marchandon, M., Vergnolle, M., Sudhaus, H., & Cavalié, O. (2018). Fault Geometry and Slip Distribution at Depth of the 1997 Mw 7.2 Zirkuh Earthquake: Contribution of Near-Field Displacement Data. *Journal of Geophysical Research: Solid Earth*, *123*(2), 1904–1924. doi: 10.1002/2017JB014703

Marone, C. (1998). Laboratory-Derived Friction Laws and Their Application to Seismic Faulting. *Annual Review of Earth and Planetary Sciences*, *26*, 643-696. doi: 10.1146/annurev.earth.26.1.643

Marone, C. J., Scholtz, C. H., & Bilham, R. (1991). On the mechanics of earthquake afterslip. *Journal of Geophysical Research: Solid Earth*, *96*(B5), 8441-8452. doi: 10.1029/91JB00275

Milliner, C. W. D., Dolan, J. F., Hollingsworth, J., Leprince, S., Ayoub, F., & Sammis, C. G. (2015, May). Quantifying near-field and off-fault deformation patterns of the 1992 M_w 7.3 Landers earthquake. *Geochemistry, Geophysics, Geosystems*, *16*(5), 1577-1598. doi: 10.1002/2014GC005693

Nagorsen-Rinke, S., Lee, J., & Calvert, A. (2013). Pliocene sinistral slip across the Adobe Hills, eastern California–western Nevada: Kinematics of fault slip transfer across the Mina deflection. *Geosphere*, *9*(1), 37–53.

Nissen, E., Elliott, J. R., Sloan, R. A., Craig, T. J., Funning, G. J., Hutko, A., ... Wright, T. J. (2016). Limitations of rupture forecasting exposed by instantaneously triggered earthquake doublet. *Nature Geoscience*, *9*(4), 330–336. doi: 10.1038/ngeo2653

Okada, Y. (1985). Surface deformation due to shear and tensile faults in a half-space. *Bulletin of the Seismological Society of America*, *75*(4), 1135–1154.

Oldow, J. S. (2003). Active transtensional boundary zone between the western Great Basin and Sierra Nevada block, western U.S. Cordillera. *Geology*, *31*(12), 1033. doi: 10.1130/G19838.1

Oldow, J. S., Geissman, J. W., & Stockli, D. F. (2008). Evolution and Strain Reorganization within Late Neogene Structural Stepovers Linking the Central Walker Lane and Northern Eastern California Shear Zone, Western Great Basin. *International Geology Review*, *50*(3), 270–290. doi: 10.2747/0020-6814.50.3.270

Oldow, J. S., Kohler, G., & Donelick, R. A. (1994). Late Cenozoic extensional transfer in the Walker Lane strike-slip belt, Nevada. *Geology*, *22*(7), 637. doi: 10.1130/0091-7613(1994)022\textless{}0637:LCETIT\textgreater{}2.3.CO;2

Oskin, M. E., Arrowsmith, J. R., Corona, A. H., Elliott, A. J., Fletcher, J. M., Fielding, E. J., ... Teran, O. J. (2012). Near-Field Deformation from the El Mayor-Cucapah Earthquake Revealed by Differential LIDAR. *Science*, *335*(6069), 702. doi: 10.1126/science.1213778

Peacock, D. C. P., & Sanderson, D. J. (1991). Displacements, segment linkage and relay ramps in normal fault zones. *Journal of Structural Geology*, *13*(6), 721–733. doi: 10.1016/0191-8141(91)90033-F

Perrin, C., Manighetti, I., Ampuero, J. P., Cappa, F., & Gaudemer, Y. (2016). Location of largest earthquake slip and fast rupture controlled by along-strike change in fault structural maturity due to fault growth. *Journal of Geophysical Research: Solid Earth*, *121*(5), 3666–3685. doi: 10.1002/2015JB012671

Perrin, C., Waldhauser, F., & Scholz, C. H. (2021). The Shear Deformation Zone and the Smoothing of Faults With Displacement. *Journal of Geophysical Research: Solid Earth*, *126*(5), e20447. doi: 10.1029/2020JB020447

Petronis, M. S., Geissman, J. W., Oldow, J. S., & McIntosh, W. C. (2009). Late Miocene to Pliocene vertical-axis rotation attending development of the Silver Peak–Lone Mountain displacement transfer zone, west-central Nevada. In *Late Cenozoic Structure and Evolution of the Great Basin-Sierra Nevada Transition* (Vol. 447, pp. 215–253). doi: 10.1130/2009.2447(12)

Pierce, I. K. D., Wesnousky, S. G., Owen, L. A., Bormann, J. M., Li, X., & Caffee, M. (2021). Accommodation of Plate Motion in an Incipient Strike Slip System: The Central Walker Lane. *Tectonics*, *40*(2), e05612. doi: 10.1029/2019TC005612

Pitarka, A., Dalguer, L. A., Day, S. M., Somerville, P. G., & Dan, K. (2009). Numerical Study of Ground-Motion Differences between Buried-Rupturing and Surface-Rupturing Earthquakes. *Bulletin of the Seismological Society of America*, *99*(3), 1521–1537. doi: 10.1785/0120080193

Pousse-Beltran, L., Nissen, E., Bergman, E. A., Cambaz, M. D., Gaudreau, É., Karasözen, E., & Tan, F. (2020). The 2020 M_w 6.8 Elazığ (Turkey) Earthquake Reveals Rupture Behavior of the East Anatolian Fault. *Geophysical Research Letters*, *47*(13), e88136. doi: 10.1029/2020GL088136

Powers, P. M., & Jordan, T. H. (2010). Distribution of seismicity across strike-slip faults in California. *Journal of Geophysical Research: Solid Earth*, *115*(B5), B05305. doi: 10.1029/2008JB006234

Press, W. H., Teukolsky, S. A., Vetterling, W. T., & Flannery, B. P. (1992). *Downhill Simplex Method in Multidimensions. Numerical Recipes in C: The Art of Scientific Computing.* Cambridge University Press, Cambridge.

Radiguet, M., Cotton, F., Manighetti, I., Campillo, M., & Douglas, J. (2009). Dependency of Near-Field Ground Motions on the Structural Maturity of the Ruptured Faults. *Bulletin of the Seismological Society of America*, *99*(4), 2572–2581. doi: 10.1785/0120080340

Ragon, T., Sladen, A., & Simons, M. (2018, August). Accounting for uncertain fault geometry in earthquake source inversions - I: theory and simplified application. *Geophysical Journal International*, *214*(2), 1174–1190. doi: 10.1093/gji/ggy187

Robertson, E. (1983). Relationship of fault displacement to gouge and breccia thickness. *American Institute of Mining Engineering Transactions*, *274*, 1426–1432.

Rockwell, T. K., Scott, L., Dawson, T., Langridge, R., Lettis, W., & Klinger, Y. (2002). Lateral Offsets on Surveyed Cultural Features Resulting from the 1999 Izmit and Duzce Earthquakes, Turkey. *Bulletin of the Seismological Society of America*, *92*(1), 79–94. doi: 10.1785/0120000809

Rood, D. H., Burbank, D. W., Herman, S. W., & Bogue, S. (2011). Rates and timing of vertical-axis block rotations across the central Sierra Nevada-Walker Lane transition in the Bodie Hills, California/Nevada. *Tectonics*, *30*(5), TC5013. doi: 10.1029/2010TC002754

Roten, D., Olsen, K. B., & Day, S. M. (2017, August). Off-fault deformations and shallow slip deficit from dynamic rupture simulations with fault zone plasticity. *Geophysical Research Letters*, *44*(15), 7733–7742. doi: 10.1002/2017GL074323

Ruhl, C. J., Morton, E. A., Bormann, J. M., Hatch-Ibarra, R., Ichinose, G., & Smith, K. D. (2021). Complex Fault Geometry of the 2020 M_{WW} 6.5 Monte Cristo Range, Nevada Earthquake Sequence. *Seismological Research Letters*, *92*(3), 1876–1890. doi: 10.1785/0220200345

Savage, H. M., & Brodsky, E. E. (2011). Collateral damage: Evolution with displacement of fracture distribution and secondary fault strands in fault damage zones. *Journal of Geophysical Research: Solid Earth*, *116*(B3), B03405. doi: 10.1029/2010JB007665

Scholz, C. H. (1987). Wear and gouge formation in brittle faulting. *Geology*, *15*(6), 493–495. doi: 10.1130/0091-7613(1987)15\textless{}493:WAGFIB\textgreater{}2.0.CO;2

Schwartz, D. P., & Coppersmith, K. J. (1984). Fault behavior and characteristic earthquakes: Examples from the Wasatch and San Andreas Fault Zones. *Journal of Geophysical Research: Solid Earth*, *89*(B7), 5681–5698. doi: 10.1029/JB089iB07p05681

Scott, C., Champenois, J., Klinger, Y., Nissen, E., Maruyama, T., Chiba, T., & Arrowsmith, R. (2019). The 2016 M7 Kumamoto, Japan, Earthquake Slip Field Derived From a Joint Inversion of Differential Lidar Topography, Optical Correlation, and InSAR Surface Displacements. *Geophysical Research Letters*, *46*(12), 6341-6351. doi: 10.1029/2019GL082202

Scott, C. P., Arrowsmith, J. R., Nissen, E., Lajoie, L., Maruyama, T., & Chiba, T. (2018, July). The M7 2016 Kumamoto, Japan, Earthquake: 3-D Deformation Along the Fault and Within the Damage Zone Constrained From Differential Lidar Topography. *Journal of Geophysical Research: Solid Earth*, *123*(7), 6138–6155. doi: 10.1029/2018JB015581

Shipton, Z. K., & Cowie, P. A. (2001). Damage zone and slip-surface evolution over μm to km scales in high-porosity Navajo sandstone, Utah. *Journal of Structural Geology*, *23*(12), 1825–1844. doi: 10.1016/S0191-8141(01)00035-9

Silver, E. A., McCaffrey, R., & Smith, R. B. (1983). Collision, rotation, and the initiation of subduction in the evolution of Sulawesi, Indonesia. *Journal of Geophysical Research: Solid Earth*, *88*(B11), 9407–9418. doi: 10.1029/JB088iB11p09407

Simons, M., Fialko, Y., & Rivera, L. (2002). Coseismic Deformation from the 1999 Mw 7.1 Hector Mine, California, Earthquake as Inferred from InSAR and GPS Observations. *Bulletin of the Seismological Society of America*, *92*(4), 1390–1402. doi: 10.1785/0120000933

Socquet, A., Hollingsworth, J., Pathier, E., & Bouchon, M. (2019). Evidence of supershear during the 2018 magnitude 7.5 Palu earthquake from space geodesy. *Nature Geoscience*, *12*(3), 192–199. doi: 10.1038/s41561-018-0296-0

Speed, R. C., & Cogbill, A. H. (1979). Candelaria and other left-oblique slip faults of the Candelaria region, Nevada. *Geological Society of America Bulletin*, *90*(2), 149. doi: 10.1130/0016-7606(1979)90\textless{}149:CAOLSF\textgreater{}2.0.CO;2

Stewart, J. H., & Ernst, W. G. (1988). Tectonics of the Walker Lane belt, western Great Basin: Mesozoic and Cenozoic deformation in a zone of shear. *Metamorphism and crustal evolution of the western United States*, *7*, 683–713.

Stirling, M. W., Wesnousky, S. G., & Shimazaki, K. (1996). Fault trace complexity, cumulative slip, and the shape of the magnitude-frequency distribution for strike-slip faults: a global survey. *Geophysical Journal International*, *124*(3), 833–868. doi: 10.1111/j.1365-246X.1996.tb05641.x

Teran, O. J., Fletcher, J. M., Oskin, M. E., Rockwell, T. K., Hudnut, K. W., Spelz, R. M., … Morelan, A. E. (2015). Geologic and structural controls on rupture zone fabric: A field-based study of the 2010 Mw 7.2 El Mayor-Cucapah earthquake surface rupture. *Geosphere*, *11*(3), 899–920. doi: 10.1130/GES01078.1

Thakur, P., & Huang, Y. (2021). Influence of Fault Zone Maturity on Fully Dynamic Earthquake Cycles. *Geophysical Research Letters*, *48*(17), e94679. doi: 10.1029/2021GL094679

Thomas, M. Y., Avouac, J.-P., Champenois, J., Lee, J.-C., & Kuo, L.-C. (2014). Spatiotemporal evolution of seismic and aseismic slip on the Longitudinal Valley Fault, Taiwan. *Journal of Geophysical Research: Solid Earth*, *119*(6), 5114-5139. doi: 10.1002/2013JB010603

Tong, X., Sandwell, D. T., & Fialko, Y. (2010). Coseismic slip model of the 2008 Wenchuan earthquake derived from joint inversion of interferometric synthetic aperture radar, GPS, and field data. *Journal of Geophysical Research: Solid Earth*, *115*(B4), B04314. doi: 10.1029/2009JB006625

Vallage, A., Klinger, Y., Grandin, R., Bhat, H. S., & Pierrot-Deseilligny, M. (2015). Inelastic surface deformation during the 2013 Mw 7.7 Balochistan, Pakistan, earthquake. *Geology*, *43*(12), 1079–1082. doi: 10.1130/G37290.1

Şengör, A. M. C., Tüysüz, O., Imren, C., Sakinç, M., Eyidoğan, H., Görür, N., … Rangin, C. (2005). The North Anatolian Fault: a New Look. *Annual Review of Earth and Planetary Sciences*, *33*, 37–112. doi: 10.1146/annurev.earth.32.101802.120415

Walker, R. T., Bergman, E. A., Elliott, J. R., Fielding, E. J., Ghods, A. R., Ghoraishi, M., … Walters, R. J. (2013). The 2010-2011 South Rigan (Baluchestan) earthquake sequence and its implications for distributed deformation and earthquake hazard in southeast Iran. *Geophysical Journal International*, *193*(1), 349-374. doi: 10.1093/gji/ggs109

Walker, R. T., Bergman, E. A., Szeliga, W., & Fielding, E. J. (2011, December). Insights into the 1968-1997 Dasht-e-Bayaz and Zirkuh earthquake sequences, eastern Iran, from calibrated relocations, InSAR and high-resolution satellite imagery. *Geophysical Journal International*, *187*(3), 1577-1603.

Walsh, J. J., & Watterson, J. (1988, January). Analysis of the relationship between displacements and dimensions of faults. *Journal of Structural Geology*, *10*(3), 239–247. doi: 10.1016/0191-8141(88)90057-0

Wang, K., Zhu, Y., Nissen, E., & Shen, Z.-K. (2021, June). On the Relevance of Geodetic Deformation Rates to Earthquake Potential. *Geophysical Research Letters*, *48*(11), e93231. doi: 10.1029/2021GL093231

Wang, S., Fan, C., Wang, G., & Wang, E. (2008, March). Late Cenozoic deformation along the northwestern continuation of the Xianshuihe fault system, Eastern Tibetan Plateau. *Geological Society of America Bulletin*, *120*(3-4), 312–327. doi: 10.1130/B25833.1

Wechsler, N., Ben-Zion, Y., & Christofferson, S. (2010, August). Evolving geometrical heterogeneities of fault trace data. *Geophysical Journal International*, *182*(2), 551-567. doi: 10.1111/j.1365-246X.2010.04645.x

Wegnüller, U., Werner, C., Strozzi, T., Wiesmann, A., Frey, O., & Santoro, M. (2016). Sentinel-1 support in the gamma software. *Procedia Computer Science*, *100*, 1305–1312. doi: 10.1016/j.procs.2016.09.246

Wesnousky, S. G. (1988, September). Seismological and structural evolution of strike-slip faults. *Nature*, *335*(6188), 340-343. doi: 10.1038/335340a0

Wesnousky, S. G. (2005, June). Active faulting in the Walker Lane. *Tectonics*, *24*(3). doi: 10.1029/2004TC001645

Wesnousky, S. G. (2006). Predicting the endpoints of earthquake ruptures. *Nature*, *444*(7117), 358–360. doi: 10.1038/nature05275

Wessel, P., Luis, J. F., Uieda, L., Scharroo, R., Wobbe, F., Smith, W. H. F., & Tian, D. (2019). The Generic Mapping Tools Version 6. *Geochemistry, Geophysics, Geosystems*, *20*(11), 5556–5564. doi: 10.1029/2019GC008515

Wetterauer, R. H. (1977). *The Mina deflection—A new interpretation based on the history of the Lower Jurassic Dunlap Formation, western Nevada* (Unpublished doctoral dissertation). Northwestern University, Evanston, Illinois.

Wright, T. J., Lu, Z., & Wicks, C. (2003). Source model for the M$_w$ 6.7, 23 October 2002, Nenana Mountain Earthquake (Alaska) from InSAR. *Geophysical Research Letters*, *30*(18), 1974. doi: 10.1029/2003GL018014

Wright, T. J., Lu, Z., & Wicks, C. (2004). Constraining the Slip Distribution and Fault Geometry of the M_w 7.9, 3 November 2002, Denali Fault Earthquake with Interferometric Synthetic Aperture Radar and Global Positioning System Data. *Bulletin of the Seismological Society of America*, *94*(6B), S175-S189. doi: 10.1785/0120040623

Wright, T. J., Parsons, B. E., Jackson, J. A., Haynes, M., Fielding, E. J., England, P. C., & Clarke, P. J. (1999). Source parameters of the 1 October 1995 Dinar (Turkey) earthquake from SAR interferometry and seismic bodywave modelling. *Earth and Planetary Science Letters*, *172*(1–2), 23–37. doi: 10.1016/S0012-821X(99)00186-7

Xiong, W., Yu, P., Chen, W., Liu, G., Zhao, B., Nie, Z., & Qiao, X. (2022). The 2020 M$_w$ 6.4 Petrinja earthquake: a dextral event with large coseismic slip highlights a complex fault system in northwestern Croatia. *Geophysical Journal International*, *228*(3), 1935-1945. doi: 10.1093/gji/ggab440

Xu, X., Sandwell, D. T., Ward, L. A., Milliner, C. W. D., Smith-Konter, B. R., Fang, P., & Bock, Y. (2020). Surface deformation associated with fractures near the 2019 Ridgecrest earthquake sequence. *Science*, *370*(6516), 605–608. doi: 10.1126/science.abd1690

Xu, X., Tong, X., Sandwell, D. T., Milliner, C. W., Dolan, J. F., Hollingsworth, J., ... Ayoub, F. (2016). Refining the shallow slip deficit. *Geophysical Journal International*, *204*(3), 1843–1862. doi: 10.1093/gji/ggv563

Yang, H., Wang, D., Guo, R., Xie, M., Zang, Y., Wang, Y., ... Zhang, Y. (2022).

Rapid report of the 8 January 2022 M_s 6.9 Menyuan earthquake, Qinghai, China. *Earthquake Research Advances*, *2*(1), 100113. doi: 10.1016/j.eqrea.2022.100113

Yang, H., & Yao, S. (2021). Shallow destructive earthquakes. *Earthquake Science*, *34*(1), 15–24. doi: 10.29382/eqs-2020-0072

Yang, J., Zhu, H., Lay, T., Niu, Y., Ye, L., Lu, Z., … Li, Z. (2021). Multifault Opposing Dip Strike Slip and Normal Fault Rupture During the 2020 M_w 6.5 Stanley, Idaho Earthquake. *Geophysical Research Letters*, *48*(10), e92510. doi: 10.1029/2021GL092510

Yang, Y. H., Tsai, M. C., Hu, J. C., Aurelio, M. A., Hashimoto, M., Escudero, J. A., … Chen, Q. (2018). Coseismic Slip Deficit of the 2017 Mw 6.5 Ormoc Earthquake That Occurred Along a Creeping Segment and Geothermal Field of the Philippine Fault. *Geophysical Research Letters*, *45*(6), 2659–2668. doi: 10.1002/2017GL076417

Yao, S., & Yang, H. (2022, January). Hypocentral dependent shallow slip distribution and rupture extents along a strike-slip fault. *Earth and Planetary Science Letters*, *578*, 117296. doi: 10.1016/j.epsl.2021.117296

Zhang, H., Thurber, C., & Bedrosian, P. (2009). Joint inversion for Vp, Vs, and Vp/Vs at SAFOD, Parkfield, California. *Geochemistry, Geophysics, Geosystems*, *10*(11), Q11002. doi: 10.1029/2009GC002709

Zheng, A., Chen, X., & Xu, W. (2020). Present-Day Deformation Mechanism of the Northeastern Mina Deflection Revealed by the 2020 M_w 6.5 Monte Cristo Range Earthquake. *Geophysical Research Letters*, *47*(22), e90142. doi: 10.1029/2020GL090142

Zinke, R., Dolan, J. F., Van Dissen, R., Grenader, J. R., Rhodes, E. J., McGuire, C. P., … Hatem, A. E. (2015, November). Evolution and progressive geomorphic manifestation of surface faulting: A comparison of the Wairau and Awatere faults, South Island, New Zealand. *Geology*, *43*(11), 1019-1022. doi: 10.1130/G37065.1

Zinke, R., Hollingsworth, J., & Dolan, J. F. (2014). Surface slip and off-fault deformation patterns in the 2013 M_W 7.7 Balochistan, Pakistan earthquake: Implications for controls on the distribution of near-surface coseismic slip. *Geochemistry, Geophysics, Geosystems*, *15*(12), 5034–5050. doi: 10.1002/2014GC005538

Supporting Information for "The 2020 M_w 6.5 Monte Cristro Range (Nevada) earthquake: anatomy of a large rupture through a region of highly-distributed faulting"

I. Sethanant[1], E. Nissen[1], L. Pousse-Beltran[1,2], E. Bergman[3], I. Pierce[4]

[1]School of Earth and Ocean Sciences, University of Victoria, British Columbia, Canada

[2]Institut des Sciences de la Terre, Université Grenoble Alpes, Université Savoie Mont Blanc, CNRS, IRD, 38000 Grenoble, France

[3]Global Seismological Services, Golden, Colorado, USA

[4]Department of Earth Sciences, University of Oxford, United Kingdom

Contents of this file

Additional Supporting Information (Files uploaded separately)

Corresponding author: I. Sethanant, School of Earth and Ocean Sciences, University of Victoria, British Columbia, Canada. (isethanant@uvic.ca)

1. Data file C1: Parameters of the distributed slip model sub-fault patches
2. Data file C2: *mloc* calibrated hypocenters
3. Data file C3: Regional moment tensor solutions

Introduction The Supplementary Information includes five figures (Figures A1–A5), one table (Figure B1), and three long tables (Tables C1–C3) uploaded separately. The figures show additional results from the InSAR-GNSS inversion and seismological modeling. Tables in the Supplementary Information and data files include the velocity model used in the earthquake relocation, and the full modeling results.

References

Blewitt, G., Hammond, W. C., & Kreemer, C. (2018). Harnessing the GPS data explosion for interdisciplinary science. *Eos*, *99*(10.1029), 485. doi: 10.1029/2018EO104623

Kennett, B. L. N., Engdahl, E. R., & Buland, R. (1995). Constraints on seismic velocities in the Earth from traveltimes. *Geophysical Journal International*, *122*(1), 108–124. doi: 10.1111/j.1365-246X.1995.tb03540.x

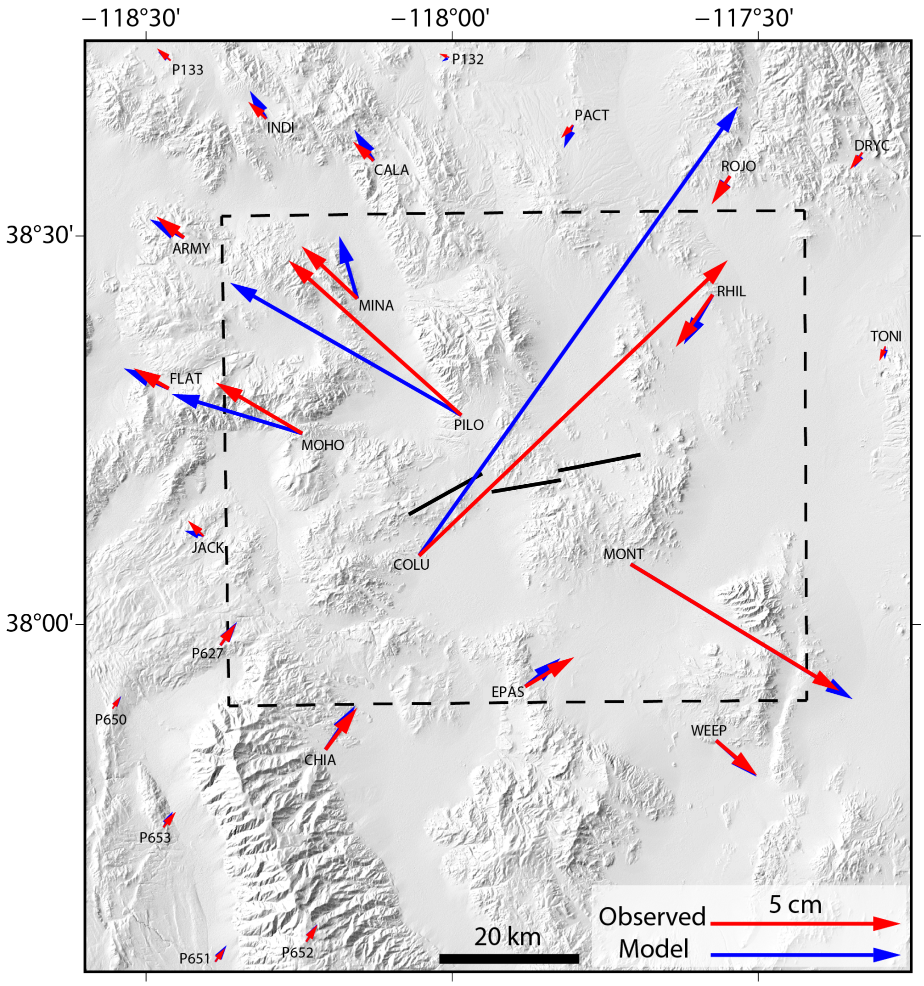

Figure A1. Observed GNSS coseismic surface displacements (red vectors, labeled with station names), processed by the Nevada Geodetic Laboratory as of 19 June 2020 (Blewitt et al., 2018), and our InSAR-GNSS distributed slip model surface displacements at the same locations (blue vectors). Thick black lines show the surface projections of our preferred three model faults. The dashed box indicates the boundary of Figure 2. See Sections 3.1 and 3.2 for further details. Station locations and coseismic offsets can be found at http://geodesy.unr.edu/news_items/20200619/nn00725272_24hr_19-Jun-2020.txt.

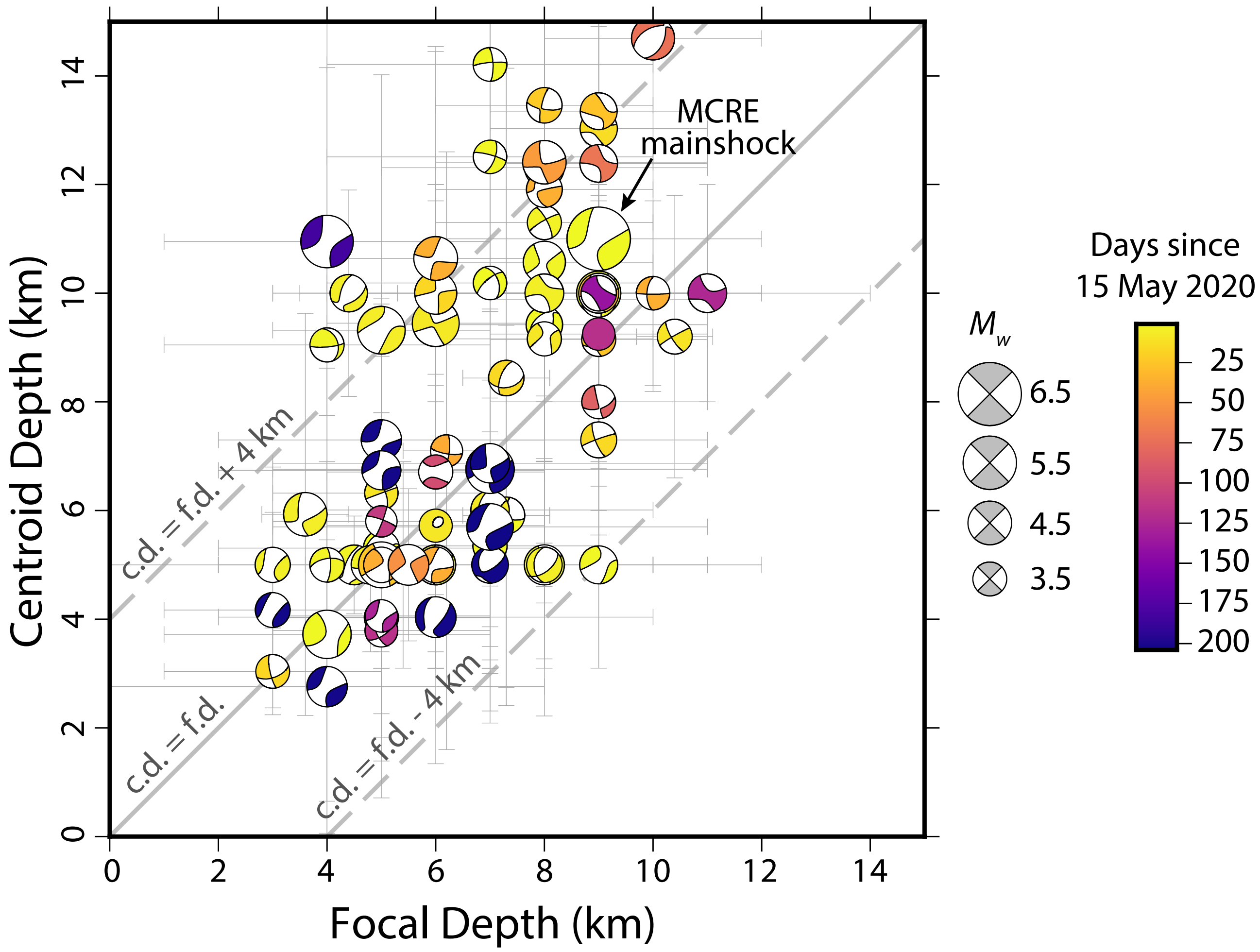

Figure A2. Comparison of centroid and focal depths of the 90 best-recorded events of the MCRE sequence (including the mainshock), calculated from regional waveform modeling and calibrated multi-event relocations, respectively (see Sections 3.3 and 3.4 for further details). The focal mechanisms are shaded by the number of days since 15 May 2020 (the mainshock), scaled by moment magnitude, with estimated uncertainty ranges as thin gray bars. The thicker gray line represents equality of centroid depths (c.d.) and focal depths (f.d.), and dashed gray lines denote 4 km offsets between the two.

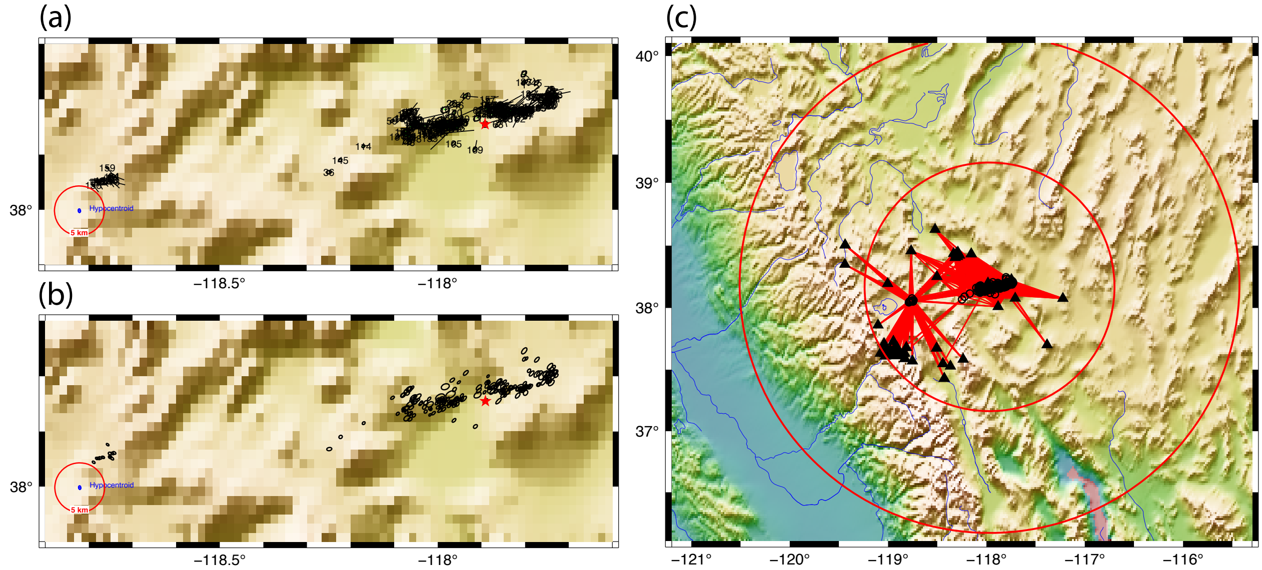

Figure A3. (a) Relocated epicenters (event numbers) and cluster vectors (black lines) showing the shift from starting locations to final, relative relocations. The red circle is a 5 km radius scale. (b) Similar to panel (a) but with 90% confidence ellipses. (c) Raypaths used for the direct calibration (absolute locations). Open circles are calibrated epicenters, black triangles are seismic stations, and red vectors are raypaths used for direct calibration. The two red circles show 1.0° and 2.0° radii centered upon the cluster hypocentroid. See https://seismo.com/mloc/summary-plots/ for more details.

Table B1. 1-D velocity model used in the *mloc* relocation, with customized phase velocities for the crust and upper mantle (<120 km) and the ak135 global model used below 120 km (Kennett et al., 1995). The Moho depth is at 30 km.

Depth range (km)	P (km/s)	S (km/s)
0.00–10.00	5.90	3.30
10.00–30.00	6.35	3.65
30.00–77.50	7.950	4.48–4.49
77.50–120.00	7.95–8.05	4.49–4.50

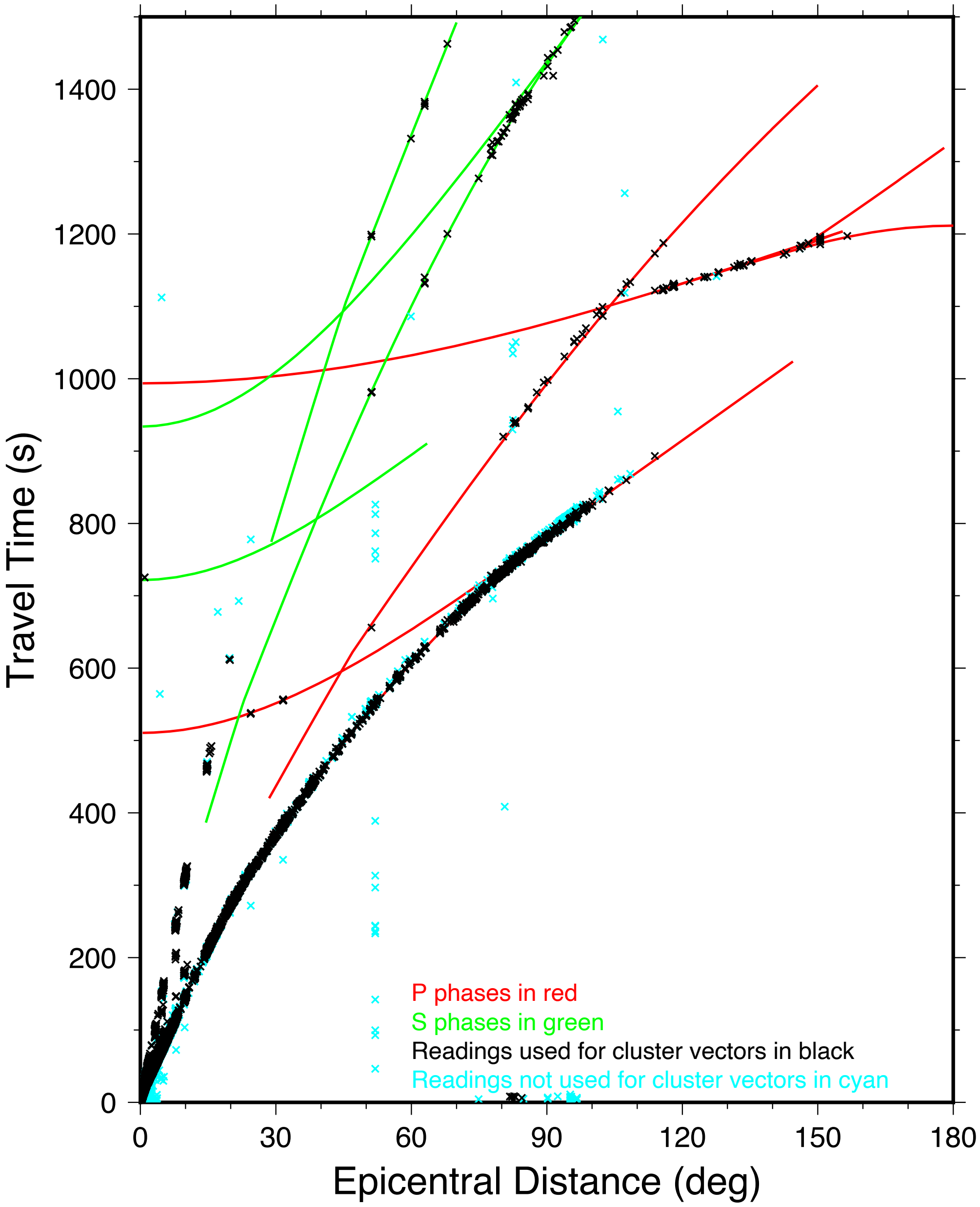

Figure A4. Theoretical and observed arrival times. Theoretical curves are from the ak135 global model (Kennett et al., 1995). The cross symbols are individual arrival time data, colored by their usage in the relocation: black—travel times used for cluster vectors but not for hypocentroid; cyan—travel times neither used for cluster vectors nor hypocentroid.

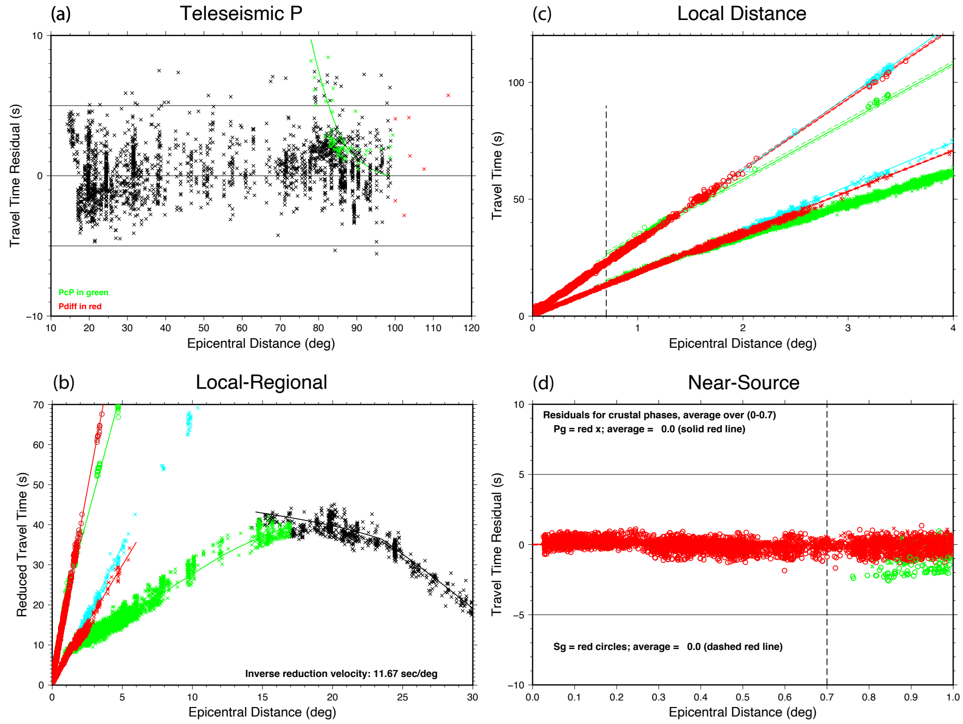

Figure A5. Arrival times at various epicentral distance ranges. (a) P phase arrivals (black crosses) from 10°–120°, reduced to the theoretical time (ak135, (Kennett et al., 1995)). The green line denotes the theoretical arrival time of phase PcP. (b) Travel times up to an epicentral distance of 30°, and reduced for visual readability (11.67 seconds/degree in inverse form, or 350 seconds at 30°). The phases include: red crosses—Pg and Sg; blue crosses—Pb and Sb; green crosses—Pn and Sn; black crosses—P; cyan circles—any other phases. (c) Travel times over 0°–4° epicentral distances. The theoretical travel times are based on the customized velocity model in Supplementary Table B1. The phases include: red crosses—Pg; blue crosses—Pb; green crosses—Pn; red circles—Sg; blue circles—Sb; green circles—Sn; cyan circles—any other phases. The vertical dashed line denotes the distance limit used to calculate the hypocentroid. (d) The residual for each arrival time within the epicentral distance used for estimating the hypocentroid, illustrated by the vertical dashed line at 0.7°. The solid and dashed red lines represent the average travel time residual for each phase. The green circles beyond the 0.7° mark is phase Sn.

Table C1. Parameters of the InSAR-GNSS distributed slip model sub-fault patches. The header is row 1; the patches of the western, central, and eastern model faults span rows 2–49, 50–77, and 78–104, respectively (see Table 2 for strike, dip, and rake values for each model fault). Each patch is 2 km $\times$ 2 km. Eastings and northings refer to the central coordinates of each sub-fault patch's surface projection.

Table C2. *mloc* calibrated hypocenters of the mainshock and 196 aftershocks. The relocated hypocentral values include the origin date, origin time, epicentral latitude and longitude, and focal depth. The depth code refers to the methods and/or data source of the focal depth estimation: m—mloc free parameter solution, n—near-source readings, l—local-distance readings. For free depth solutions, the uncertainties in depth are calculated from the covariance matrix of the relocation. For manually fixed depths, the uncertainties are estimated from observations and trials to be ± 2 km and ± 3 km for the depth codes n and l, respectively. The ellipse semi-axis azimuth ($^\circ$) and length (km) reflect the uncertainties in the epicenter location. The short semi-axis azimuth is implied (perpendicular to the long semi-axis). The earthquake magnitude is gathered from the ISC bulletin and ANSS ComCat. Further information of *mloc* direct calibration output and depth constraints can be found at https://seismo.com/mloc/hdf-files/ and https://seismo.com/mloc/depth-constraint/.

Table C3. Regional moment tensor solutions for the 90 best-recorded events. We model the regional waveforms and invert for the moment magnitude, centroid depths, the six moment tensor components, and the two possible nodal planes of the focal mechanism. The origin date, origin time, and epicentral latitude and longitude are gathered from NEIC. The moment tensor components (mrr, mtt, mpp, mrt, mrp, mtp) are in N m units. The last column ('source') refers to the data source (us—NEIC; nn—UNR) and phase type used in the inversion (Mwr—whole seismogram; Mww—W-phase). See Section 3.4 for full details of the waveform modeling.